

Ultrafast Frustration-Breaking and Magnetophononic Driving of Singlet Excitations in a Quantum Magnet

F. Giorgianni,^{1,2} B. Wehinger,^{1,3,4} S. Allenspach,^{1,3} N. Colonna,^{1,5} C. Vicario,¹
P. Puphal,^{1,6} E. Pomjakushina,¹ B. Normand,^{1,7,8} and Ch. Rüegg^{1,3,8,9}

¹*Paul Scherrer Institute, CH-5232 Villigen-PSI, Switzerland*

²*Institute of Applied Physics, University of Bern, CH-3012 Bern, Switzerland*

³*Department of Quantum Matter Physics, University of Geneva, CH-1211 Geneva 4, Switzerland*

⁴*European Synchrotron Radiation Facility, 71 Av. des Martyrs, 38000 Grenoble, France*

⁵*National Centre for Computational Design and Discovery of Novel Materials (MARVEL),
Ecole Polytechnique Fédérale de Lausanne (EPFL), CH-1015 Lausanne, Switzerland*

⁶*Max Planck Institute for Solid State Research, Heisenbergstrasse 1, 70569 Stuttgart, Germany*

⁷*Lehrstuhl für Theoretische Physik I, Technische Universität Dortmund,
Otto-Hahn-Strasse 4, 44221 Dortmund, Germany*

⁸*Institute of Physics, Ecole Polytechnique Fédérale de Lausanne (EPFL), CH-1015 Lausanne, Switzerland*

⁹*Institute of Quantum Electronics, ETH Zürich, CH-8093 Hönggerberg, Switzerland*

Ideal magnetic frustration forms the basis for the emergence of exotic quantum spin states that are entirely nonmagnetic. Such singlet spin states are the defining feature of the Shastry-Sutherland model, and of its faithful materials realization in the quantum antiferromagnet $\text{SrCu}_2(\text{BO}_3)_2$. To address these states on ultrafast timescales, despite their lack of any microscopic order parameter, we introduce a nonlinear magnetophononic mechanism to alter the quantum spin dynamics by driving multiple optical phonon modes coherently and simultaneously. We apply intense terahertz pulses to create a nonequilibrium modulation of the magnetic interactions that breaks the ideal frustration of $\text{SrCu}_2(\text{BO}_3)_2$, such that previously forbidden physics can be driven in a coherent manner. Specifically, this driving populates a purely magnetic excitation, the singlet branch of the two-triplon bound state, by resonance with the difference frequency of two pumped phonons. Our results demonstrate how light-driven phonons can be used for the ultrafast and selective manipulation of interactions in condensed matter, even at frequencies far from those of the pump spectrum, offering valuable additional capabilities for the dynamical control of quantum many-body phenomena.

I. INTRODUCTION

Using ultrafast lasers to access all the intrinsic interaction timescales of correlated quantum materials opens a new window on fundamental processes in nonequilibrium many-body physics. Coherent light sources developed to combine ultrafast time structure and high intensity at the appropriate terahertz (THz) or infrared (IR) frequencies [1, 2] have been used in complex condensed matter to enhance superconductivity [3], drive metal-insulator transitions [4], manipulate multiferroic order [5], and “Floquet engineer” the electronic band structure [6]. This type of dynamical driving, by which different and unconventional static and dynamic properties are conferred on a quantum state, has the potential to reveal many previously hidden or unknown phenomena [7, 8].

In ultrafast magnetism, the magnetic field of a light pulse can drive precessional spin dynamics and spin waves in ordered antiferromagnets [9, 10], while the electric field can modify the magnetic interactions [11]. Strong lattice excitations have been used to melt magnetic order [12] and to induce spin waves through an effective magnetic field [13]. The concept of magnetophononics, defined as the resonant modulation of magnetic (super)exchange interactions by ultrafast coherent lattice displacements, has to date been discussed only in theory [14]. Although phononic effects observed in ordered magnetic materials have been ascribed in part to

exchange interactions [15] or fully to crystal-field effects [16], they remain some orders of magnitude slower than the driving phonons. While the ultrafast manipulation of magnetically ordered phases is developing towards applications in spintronics [17, 18], the situation in quantum magnets that lack any magnetic order remains largely unexplored.

In this work we begin the quest to control the properties of nonordered quantum magnetic materials using ultrafast coherent light pulses. The paradigm of ideal frustration is the fundamental ingredient in all of the complex quantum many-body states in magnetism, most of which emerge from rather simple spin Hamiltonians [19]. Its most basic form is geometrical frustration, which has been realized in a wide range of materials hosting antiferromagnetically interacting spins in the triangle-based motifs of the kagome, pyrochlore, Shastry-Sutherland, and other lattices. More complex forms of ideal frustration have been produced using magnetic interactions that are anisotropic in spin or real space, examples including spin ices, $\text{SU}(N)$ magnets, and (proximate) Kitaev systems [20]. However, the characteristic properties of the resulting ground and excited states, which can include both gapped and gapless quantum spin liquids [21], fractional quasiparticles, topological order, and long-ranged entanglement [20], are often undetectable by the conventional probes of experimental condensed matter. This makes them ideal candidates for ultrafast probing.

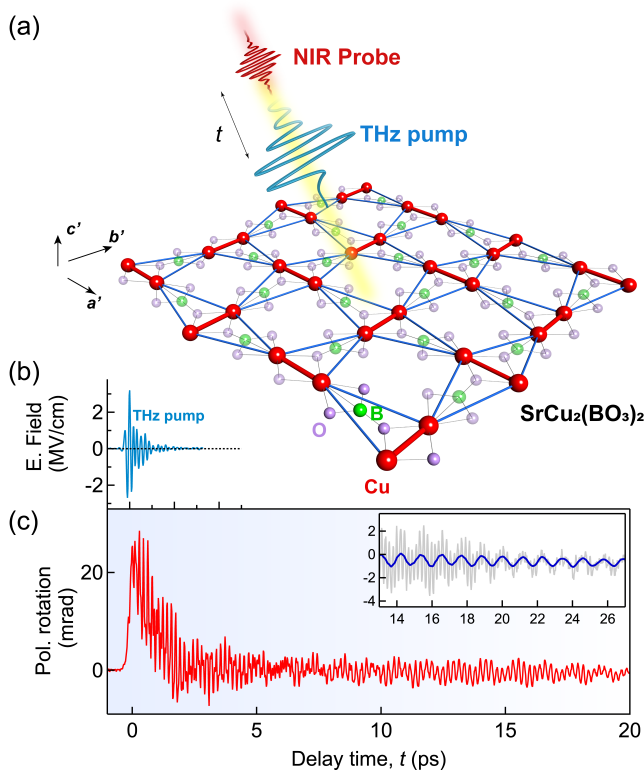


FIG. 1. **Coherent lattice control in the time domain.** (a) An intense THz pulse (blue) with electric field polarized linearly along the a' axis of a SrCu₂(BO₃)₂ crystal provides coherent driving of dipole-active lattice vibrations. A femtosecond near-IR (NIR) probe pulse (red) measures the polarization changes. (b-c) THz electric field and polarization rotation of the probe as functions of the delay time, t . Inset: THz-driven dynamics after filtering of the fast component to reveal coherent oscillations associated with the low-lying magnetic excitation (dark blue).

For our study (Fig. 1) we choose SrCu₂(BO₃)₂, an archetypal quantum magnetic material whose physics is dominated by local quantum mechanical singlet states [22]. The singlet encapsulates the essence of quantum magnetism, where the fluctuating spin variables combine into both local and global states of especially low energy that have no external magnetic properties [23]. The ideally frustrated geometry of SrCu₂(BO₃)₂ [Fig. 1(a)] realizes a spin model formulated by Shastry and Sutherland specifically for its exact dimer-singlet ground state [24], and if an applied pressure is used to alter the interaction parameters then it undergoes a first-order quantum phase transition (QPT) to a four-site “plaquette” singlet state [25–28]. This ideal magnetic frustration also causes SrCu₂(BO₃)₂ to display an anomalous spectrum of spin excitations and complex phase transitions both in an applied magnetic field [29–31] and as a function of temperature [28].

For the goal of ultrafast modulation of magnetic properties in nonordered materials such as SrCu₂(BO₃)₂, the

magnetophononic mechanism is an obvious candidate. Experiments applying static pressure to quantum magnets have created novel ground and excited states [26, 32] and have controlled QPTs in both localized [33] and itinerant magnetic systems [34], demonstrating not only the sensitivity of the magnetic interactions to the atomic positions but also the potential for qualitatively new dynamical phenomena. In our study it is important to stress the distinction between magnetophononics, which is a resonant modulation of the magnetic interactions by harmonic phonons [14], and “nonlinear phononics” [35], which exploits the anharmonic potential of large-amplitude phonons. The latter offers a route for combining phonons at their sum and difference frequencies, and the lattice distortions it allows have been applied in ordered magnets to alter their static properties [13]. The former relies on the complex dependence of the magnetic interactions on the periodically varying lattice coordinates to effect a dynamical coupling to the spin sector. We will observe both mechanisms at work in our experiments, but only the magnetophononic mechanism drives the spin sector, and thus our focus lies here.

Nevertheless, modulating an interaction, J , at some available phonon frequency, ω_i , does not constitute control of dynamical properties: *a priori* there is no match between the energy scales of the dominant IR-active phonon modes and of the elementary magnetic excitations in any material, and we will see that SrCu₂(BO₃)₂ is a case in point. To achieve such frequency matching, we extend magnetophononics to the nonlinear regime, where sums and differences of the available phonon frequencies span a wide energy range, but extremely intense electric fields are required. By using coherent THz pulses to drive IR-active phonons in SrCu₂(BO₃)₂ (Fig. 1), we demonstrate experimentally how the leading difference frequency creates a nonequilibrium occupation of the lowest excited singlet state. We establish the theoretical framework for the origin of this phenomenon, in the breaking of ideal magnetic frustration within the driven lattice structure, which we verify by density functional theory (DFT) calculations.

The structure of this article is as follows. In Sec. II we review the properties of SrCu₂(BO₃)₂. In Sec. III we present the results of our ultrafast spectroscopic investigations. Section IV contains a qualitative and quantitative account of the nonlinear magnetophononic phenomena we observe. In Sec. V we discuss the consequences of our findings for the selective static and dynamical control of materials properties both within and beyond quantum magnetism.

II. SHASTRY-SUTHERLAND MODEL AND SrCu₂(BO₃)₂

The Shastry-Sutherland model, for $S = 1/2$ spins with Heisenberg interactions on the two-dimensional orthogonal-dimer network shown in Fig. 2(a) [24], is one

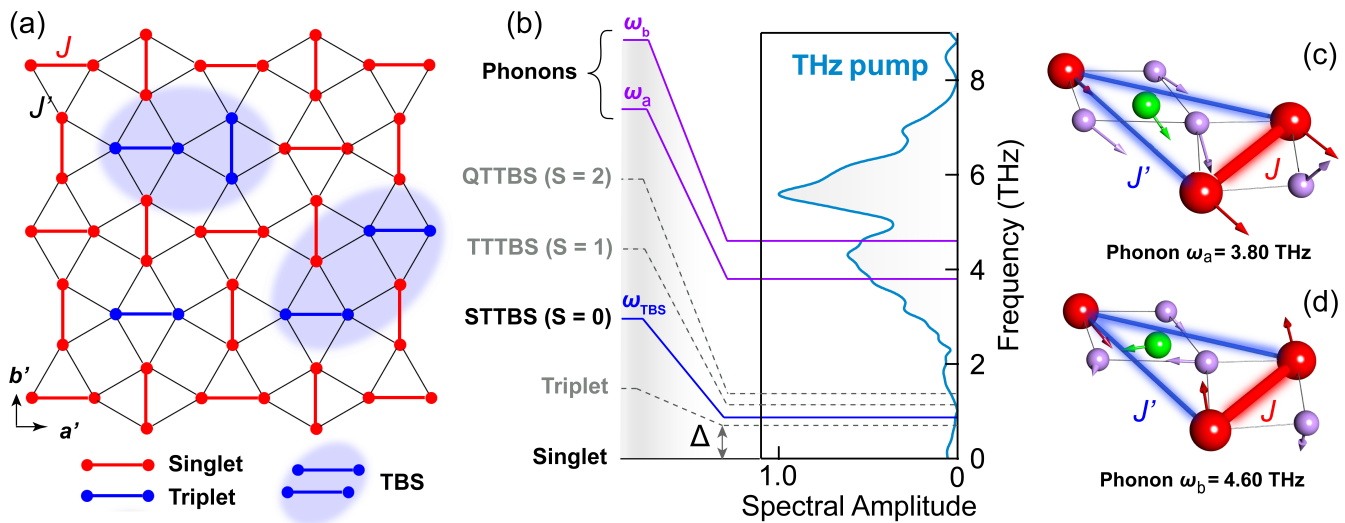


FIG. 2. **Low-energy spin and phonon modes in $\text{SrCu}_2(\text{BO}_3)_2$.** (a) Schematic representation of the spin network in $\text{SrCu}_2(\text{BO}_3)_2$, showing how Cu^{2+} ions ($S = 1/2$) form the Shastry-Sutherland geometry with interaction parameters J on the Cu-Cu dimers and J' between neighboring orthogonal dimers. The localized spin excitations above the singlet ground state (red dimers) are individual triplons (blue dimers) and two-triplon bound states (TBS, blue shaded regions). (b) Low-energy spectrum of $\text{SrCu}_2(\text{BO}_3)_2$ at $\mathbf{k} = 0$. In the spin sector, the singlet two-triplon bound state (STTBS) lies close to the one-triplon excitation, the triplet two-triplon bound state (TTTBS) has a smaller binding energy, and the quintet two-triplon bound state (QTTBS) lies close to the threshold for creating two isolated triplons (energies of the lowest TTTBS and QTTBS taken from Ref. [36]). In the lattice sector, we show the frequencies of the two phonons excited most strongly in our experiment, $\omega_a = 3.80$ THz and $\omega_b = 4.60$ THz. The light blue line and gray shading represent for comparison the amplitude of the pump spectrum [Fig. 3(a)]. (c-d) Lattice-displacement eigenvectors for the phonon modes at ω_a and ω_b ; because both phonons are E -symmetric, we show one of the two degenerate modes in each case. J and J' depend on the bond lengths and angles in the superexchange paths involving the Cu, O, and B atoms.

of the most intriguing in quantum magnetism. The exact and entirely nonmagnetic ground state of singlet quantum dimers is found when the ratio of interdimer (J') to intradimer (J) interactions satisfies $\alpha = J'/J \leq 0.675$, above which the QPT occurs to the plaquette-singlet state [25]. It is quite remarkable that this simple model is realized so faithfully in the compound $\text{SrCu}_2(\text{BO}_3)_2$ [Fig. 1(a)] [22], with J determined by Cu-O-Cu superexchange processes on the Cu^{2+} dimer units and J' by superexchange through the BO_3 units. The magnetic excitation spectrum of $\text{SrCu}_2(\text{BO}_3)_2$, depicted for wave vector $\mathbf{k} = 0$ in Fig. 2(b), contains as its lowest mode the “triplon” (singlet-triplet) excitation at $\Delta = 2.9$ meV ($\equiv 0.71$ THz), whose dispersion is almost flat in \mathbf{k} [37] as a consequence of the ideal frustration. The lattice geometry is also responsible for an anomalously strong binding energy for triplon pairs, with the result that the singlet two-triplon bound state (STTBS), the $S = 0$ branch of this multiplet, appears just above the one-triplon mode, at 3.6 meV ($\omega_{TBS} = 0.87$ THz). At higher energies, additional discrete and continuum excitations include the triplet ($S = 1$, TTTBS) and quintet ($S = 2$, QTTBS) branches of this bound state.

These modes have been studied by a combination of neutron scattering [38], which targets the triplon and TTTBS, and Raman [39, 40], IR [41], and electron spin resonance (ESR) spectroscopies [36], which observe the

spectrum at $\mathbf{k} = 0$. To date, a detailed explanation for the phonon-assisted coupling of light to the spin excitations observed by Raman and IR remains elusive due to the inherently incoherent nature of these experiments. The interaction ratio in $\text{SrCu}_2(\text{BO}_3)_2$, $\alpha = 0.63$, lies close to the QPT of the Shastry-Sutherland model, allowing this transition to be induced under pressure [26]. Recent attention has focused on how the magnetic interactions depend on the geometry of the dimer units [42–44], making $\text{SrCu}_2(\text{BO}_3)_2$ a fascinating and timely candidate for exploring ideally frustrated quantum magnetism on ultrafast timescales.

III. ULTRAFAST EXPERIMENT

We perform THz-pump, optical-probe spectroscopy using the apparatus of Ref. [45], whose technical specifications are detailed in App. A. Our experiments use a single-crystal sample of $\text{SrCu}_2(\text{BO}_3)_2$ maintained at 3.5 K ($k_B T \ll \Delta$), a temperature where the ground state is close to the pure singlet state. As represented in Fig. 1(a), intense light pulses [Fig. 1(b)] with spectral content between 2 and 7 THz [Fig. 2(b)] drive the resonant excitation of dipole-active phonon modes [46]. To estimate the external THz electric-field strength of the pump, we measured the energy per pulse, beam waist,

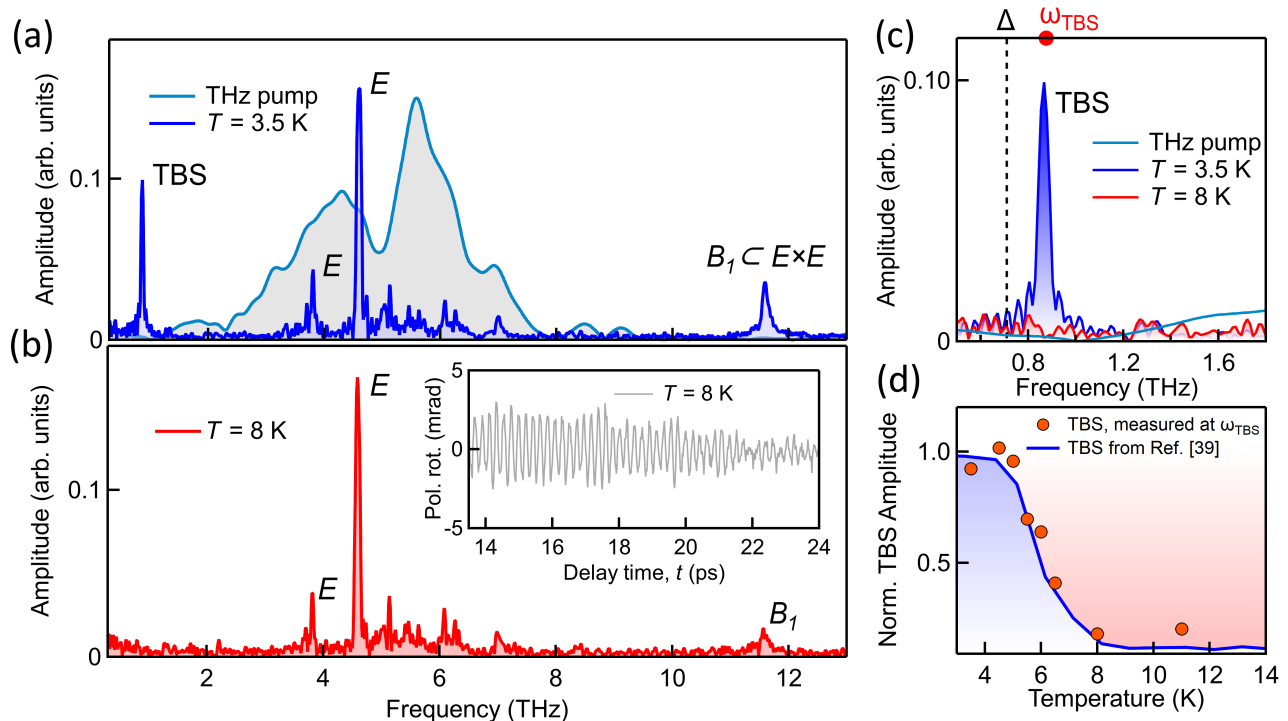


FIG. 3. **THz field-driven lattice and spin dynamics in the frequency domain.** (a) Spectral amplitude (blue) of the data of Fig. 1(c) computed for $3.5 \leq t \leq 20$ ps. The primary peaks are (i) E -symmetric phonons at 3.80 THz and 4.60 THz, (ii) a B_1 -symmetric Raman phonon at 11.6 THz, and (iii) the TBS excitation at $\omega_{\text{TBS}} = 0.87$ THz. The light blue line and gray shading show the spectral amplitude of the driving electric field [Fig. 1(b)]. (b) Spectral amplitude measured at 8 K, where the TBS is absent and the driven dynamics reveal no coherent oscillations at ω_{TBS} (inset). (c) Comparison of low-frequency spectra at 3.5 and 8 K. The black dashed line marks the one-triplon gap, $\Delta = 2.9$ meV (0.71 THz), and the red dot ω_{TBS} from Raman spectroscopy [39, 40]. (d) Temperature-dependence of the TBS, normalized to the peak height.

and pulse duration, also reported in App. A, to obtain the value $E_{\text{THz}} = 3.2 \text{ MVcm}^{-1}$, which is comparable to other modern high-intensity sources [47, 48]. To probe the driven lattice and spin dynamics, we measured the ultrafast polarization rotation [13], shown in Fig. 1(c), caused by the associated optical birefringence and Faraday effects. These are imprinted on a co-propagating NIR pulse (50 fs, wavelength 800 nm) with a variable the delay time, t , and an analysis of the complete time-frequency response function is presented in App. B.

As the inset of Fig. 1(c) makes clear, the ps pump pulse creates dynamical oscillations that persist for many tens of ps. We take this observation as an opportunity to establish our use of terminology. It is clear that all of the physical phenomena revealed by ultrafast pulsed driving are transient, in the sense that the stimulus is removed after a very short time (here 1 ps) and the system relaxes back to equilibrium. This relaxation is governed by the characteristic decay times of the multiple eigenmodes of the system, all of which are in principle excited by the wide range of frequencies present in the short pulse. It is during this time that we apply the term “nonequilibrium,” to refer to the situation where the system is in an out-of-equilibrium state, with a nonequilibrium (non-

thermal) occupation of the states in the spectrum and the possibility of changes to the eigenenergies and eigenstates of this spectrum (i.e. away from their equilibrium properties). In the following we will show that Fig. 1(c) presents a particularly clear separation of timescales, by which the phonon modes driven by the electric field of the THz pulse have largely decayed after 20 ps, but the slow oscillation they drove, which is the leading excitation in the magnetic sector, lives far longer. This consequence of the very weak coupling of spins to their environment provides an excellent illustration of our rationale for studying quantum magnetism.

Returning to our experimental observations, in the frequency domain we find coherently excited phonons close to the peak of the pump spectrum [Fig. 3(a)], primarily two of the E -symmetric modes measured by IR spectroscopy [46], centered at $\omega_a = 3.80$ and $\omega_b = 4.60$ THz. As noted above, these phonon frequencies lie far above the primary features in the magnetic spectrum. Nonetheless, we observe a striking response precisely at $\omega_{\text{TBS}} = 0.87$ THz [Fig. 3(b)], even though the spectral content of the pump is negligible in this frequency range. In the same way, the feature centered at 11.6 THz lies much higher than the spectral content of the pump, and

the appearance of this Raman-active B_1 phonon mode in the measured response indicates that nonlinear phonon mixing is allowing sum-frequency excitation processes. In fact this feature constitutes one of the clearest examples of a sum-frequency phonon excitation yet observed, and thus we analyze it in detail in App. C, but from the standpoint of magnetophononics it serves only as an indicator of the mechanism for the phenomena we investigate.

Henceforth we refer to the STTBS, whose nonmagnetic ($S = 0$) character makes it the only low-energy mode one may expect to excite strongly with phonons, simply as the TBS. To identify the excitation at 0.87 THz as the TBS, we undertook a number of tests. First we repeated the experiment at 8 K [Figs. 3(b-c)], where thermal fluctuations cause the triplons to lose their character [49]. While the spectral features of the lattice remain almost unchanged, the magnetic fingerprint of THz driving has disappeared. As Fig. 3(d) makes clear, the measured amplitude shows rapid quenching above 5 K, exactly as observed for the TBS in Ref. [39], where this behavior was attributed to strong scattering from thermally excited triplets. The loss of triplon spectral weight at a temperature so anomalously low in comparison with the 34 K gap [Fig. 2(d)] was explained only recently by the massive proliferation of bound and scattering states of two triplons as their energy increases [50], and the exact coincidence of the triplon [49] and TBS decay functions indicates the origin of the behavior we observe in Fig. 3(d) [39]. The reduced lifetime of the B_1 phonon in Fig. 3(b) also provides evidence of damping processes due to spin-lattice coupling.

To understand the mechanism driving a purely magnetic excitation, the fact that the spectral content of the pump contains negligible intensity below 2 THz excludes a direct coupling of light to the TBS, which in any case is not IR-active [41]. To probe the indirect origin of the observed spin dynamics, we measure the mode amplitudes as functions of the THz electric-field strength. These amplitudes and their uncertainties are extracted from Gaussian fitting as described in App. D. The IR phonons display the linear dependence expected for resonant excitation [Fig. 4(a)]. By contrast, the TBS amplitude varies quadratically with the field strength [Fig. 4(b)], and thus with lattice displacement, indicating a nonlinear coupling mechanism essentially different from electric or magnetic dipolar interactions [10, 51]. Confirmation that this dependence is quadratic can also be obtained from the invariance of the output signal on inverting the polarity of the pump electric field, as we show in App. E.

For a direct demonstration of which IR phonons provide the driving, we vary the spectral content of the pump by the insertion of different high- and low-pass filters, as described in App. A. The resulting pump spectra are shown in Fig. 4(c) and again the corresponding TBS amplitude, shown in Fig. 4(d), is large only when the pump spectrum covers ω_a and ω_b . There is no sign of coherent magnetic dynamics in off-resonant conditions, as we show explicitly for driving frequencies predominantly below 2

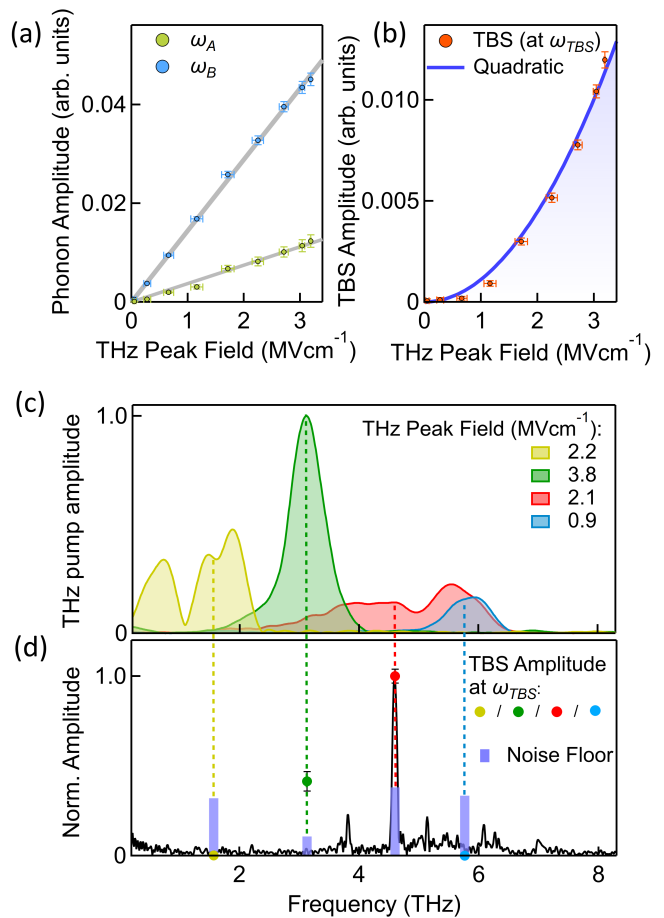


FIG. 4. **THz pump strength and frequency-dependence.** (a) Linear dependence of phonon amplitudes and (b) quadratic dependence of the TBS amplitude on the electric-field strength. (c) Four different pump spectra obtained by filtering of the THz beam and labelled by their peak field values in the time domain; dashed lines mark the centroid of each spectral envelope. (d) TBS mode amplitude (colored points), normalized to the square of the peak field, for the four different values of the THz pump-frequency centroid in panel (c). Bars mark the noise floor of the extracted signal in each case.

and above 5.5 THz.

This proves that the opto-magnetic coupling is mediated by the resonant lattice excitations. However, one may still suspect that the phonon driving is not direct, but occurs rather as a consequence of nonlinear effects involving non-resonant electronic excitations. THz-induced free-carrier generation could result in the excitation of coherent phonons by dispersive processes [52], with modes ω_a and ω_b being favored by their spectral weight, and indeed the dispersive mechanism has been the subject of some recent ultrafast studies [53, 54]. To eliminate the possibility of THz-induced free-carrier generation in $\text{SrCu}_2(\text{BO}_3)_2$, we measured the transmission modulation of the NIR probe pulse whose polarization rotation is shown in Fig. 1(c). The results of this study,

which we show in App. F, demonstrate conclusively that no free carriers are produced by our THz pump pulse, and hence that any mechanisms generating these, which include THz-induced electronic breakdown [55] or impact ionization [56, 57], are excluded in $\text{SrCu}_2(\text{BO}_3)_2$.

Focusing now on the direct driving of coherent phonons, for a quantitative analysis of the effect of the THz pulse on the atomic motions within the sample, we equate the polarization induced by the electric field with the modulation of the dipole moment, which peaks strongly when the pulse frequency is resonant with a phonon mode, denoted by m . In this situation $P_m = n_d \delta_m \mu_m$, where μ_m is the net charge displacement due to mode m , n_d is a dipole density, and δ_m is the maximum displacement coordinate of the phonon. In this way we deduce (App. A) maximum displacements up to $\delta_b = 0.17$ Å for the 4.60 THz mode [shown in Fig. 2(d)], which is comparable to the value estimated in SrTiO_3 [58]. We stress that δ_m represents the maximum displacement of the most displaced O ion in the $\text{SrCu}_2(\text{BO}_3)_2$ structure due to phonon mode m , and that the corresponding displacements of the Cu ions are generally smaller (by a factor of 3-4 for the 4.60 THz mode), whence the system does not approach the Lindemann melting criterion. Because the temporal duration of the pump pulse is approximately 0.5 ps [Fig. 1(b)], the amount of energy transferred presents little danger that the THz driving can increase the sample temperature significantly.

IV. THEORY: FRUSTRATION-BREAKING

A. Analysis

We now establish the physical framework for the nonlinear magnetophononic phenomenon we have created. Qualitatively, the lattice displacements due to any phonon excitation alter the instantaneous magnetic interactions [Fig. 5(a)]. To analyze this situation we express the Hamiltonian of the driven system as

$$H = H_0 + H_H + V_{\text{Ph}} + H_{\text{Ph-Em}} + H_D, \quad (1)$$

where H_0 is spin-independent and

$$H_H = J \sum_{\langle ij \rangle} \vec{S}_i \cdot \vec{S}_j + J' \sum_{\langle\langle ij \rangle\rangle} \vec{S}_i \cdot \vec{S}_j, \quad (2)$$

is the Shastry-Sutherland model at equilibrium: \vec{S}_i is a spin-1/2 operator located on the Cu^{2+} ion at site i , J and J' are the magnetic interactions depicted in Fig. 2(a), and $\langle ij \rangle$ and $\langle\langle ij \rangle\rangle$ denote respectively pairs of sites on intra- and interdimer bonds. V_{Ph} is the phonon potential and $H_{\text{Ph-Em}} = \sum_m \mu_m q_m E_{\text{THz}}$, the dipole coupling between the lattice and the THz light, is the term driving the excitation of IR-active phonon modes. The action of the coherent lattice deformation due to all of these phonon modes, $q_t = \sum_m q_m$, in modulating the magnetic interaction parameters causes additional coupled spin-phonon

terms to enter the Hamiltonian, which we collect in H_D . To separate the phonon modulation terms in H_D , it is convenient to perform a Taylor expansion of the magnetic interactions, J and J' , in powers of the simultaneously driven coherent IR phonon coordinates, which we denote as q_m, q_n, \dots . Denoting an arbitrary interaction term as \tilde{J} , we obtain

$$\begin{aligned} \tilde{J}(q_m, q_n, \dots) = \tilde{J}(0) &+ \left. \frac{\partial \tilde{J}}{\partial q_m} \right|_{q_m=0} q_m \\ &+ \left. \frac{\partial^2 \tilde{J}}{\partial q_m \partial q_n} \right|_{q_m, q_n=0} q_m q_n + \dots \end{aligned} \quad (3)$$

where the first term is part of H_H and the higher terms make clear the direct dependence of the additional contributions on the oscillating phonon coordinates.

Both the key features of our experiment become clear immediately in a minimal model with only two harmonic IR phonons, i.e. $q_t = q_a + q_b$, where q_a and q_b are vectors of normal-mode coordinates with cosinusoidal time structures at respective frequencies ω_a and ω_b . The q_t^2 terms appearing in the second line of Eq. (3) lead to spectral components at frequencies $2\omega_a, \omega_a + \omega_b, 2\omega_b, 0$, and $\omega_b - \omega_a$. These quadratic terms provide the leading nonlinear mechanism that allows a very wide range of spin excitation energies to be addressed using the sum and difference frequencies of driven IR phonons, whose frequency range may be more restricted.

The second key feature is that the unconventional physics of the Shastry-Sutherland model, and by extension of $\text{SrCu}_2(\text{BO}_3)_2$ at equilibrium, relies on the ideal frustration of the spin correlations between dimers. The term $\vec{S}_i \cdot \vec{S}_j$ acting on a single dimer is an eigenoperator and when acting between dimers it is exactly cancelled by a second $\vec{S}_i \cdot \vec{S}_j$ term with equal size (J') and effectively opposite sign [Fig. 2(a)]. However, the excited phonons driving the lattice out of equilibrium cause frustration-breaking in the magnetic sector, in the form of a finite interdimer coupling, $\Delta J'_{12} = J'_1(q_m, q_n, \dots) - J'_2(q_m, q_n, \dots)$ (and similarly for $\Delta J'_{34}$, $\Delta J'_{56}$, and $\Delta J'_{78}$), that connects nearest-neighbor dimers [Fig. 5(a)]. This has the immediate effect of allowing two qualitatively new types of physical process that are forbidden at equilibrium.

To make these most transparent, we reexpress the out-of-equilibrium spin Hamiltonian in terms of triplet creation and annihilation operators, which represent the excitations of the dimer (J) units in Fig. 2(a) above their singlet ground state. A full discussion of the bond-operator description may be found in Ref. [59]. Treating the singlets as a scalar term gives conventional leading-

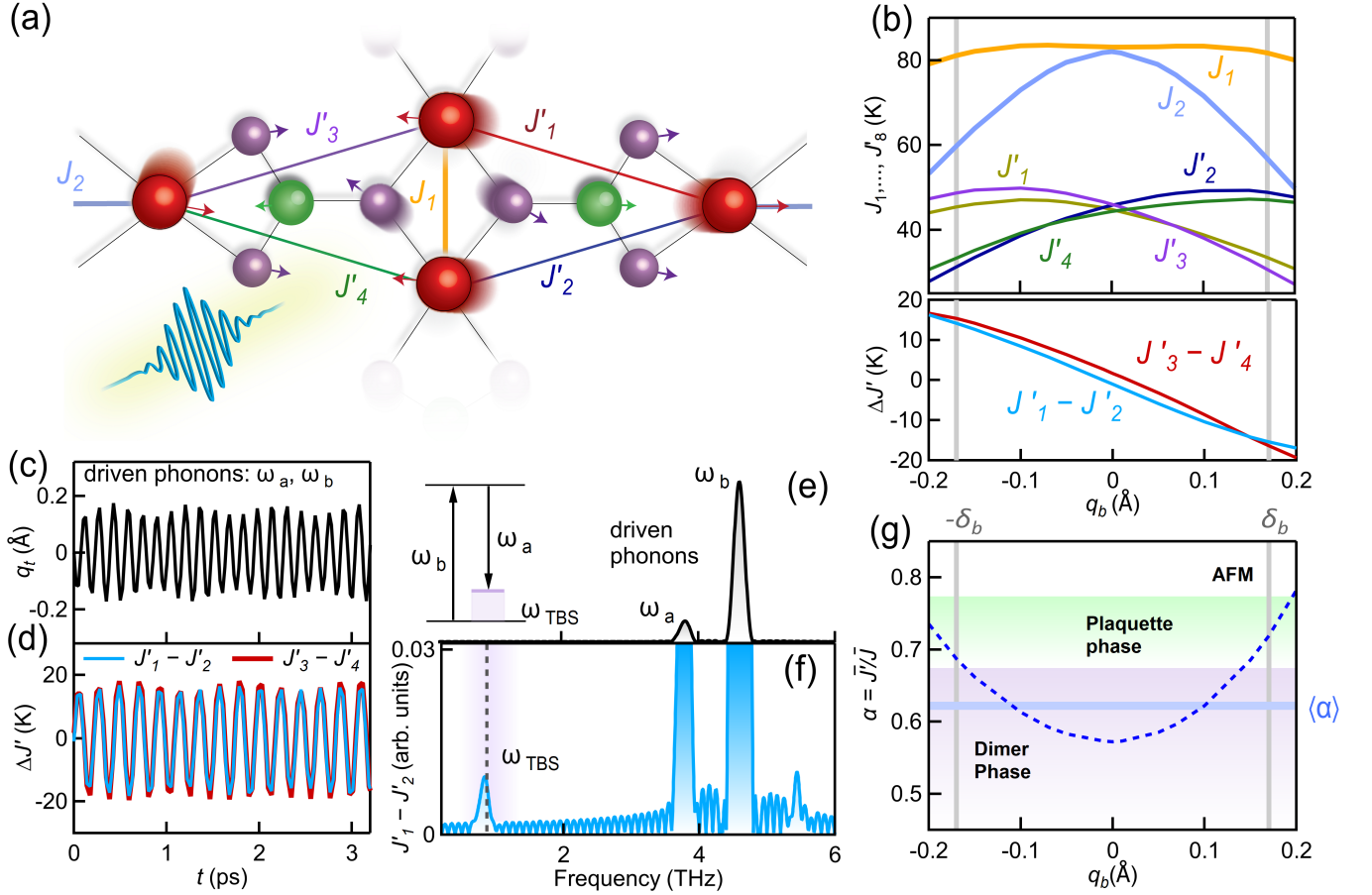


FIG. 5. **Dynamic control of magnetic interactions by light-driven phonons.** (a) Schematic representation of atomic motions in the ab -plane associated with the $\omega_b = 4.60$ THz phonon. (b) Interaction parameters $J, J'_1, J'_2, J'_3, J'_4, \Delta J'_{12}$, and $\Delta J'_{34}$ calculated for the symmetry-broken lattice structure as functions of the corresponding phonon displacement, q_b . (c) Temporal modulation of $q_a + q_b$ calculated using the experimental THz driving field. (d) Corresponding dynamic modulation of $\Delta J'_{12}$ and $\Delta J'_{34}$, which are controlled primarily by the ω_b phonon. (e) Spectrum of driven IR phonons, which shows weight only at the frequencies ω_a and ω_b . Inset: energy-level diagram of the TBS excitation process, which is a resonance between the phonon frequency difference, $\omega_b - \omega_a$, and ω_{TBS} . (f) Fourier transform of the DFT time series for $\Delta J'_{12}(t)$, which shows spectral weight at ω_{TBS} . (g) Interaction ratio, $\alpha = \bar{J}'/\bar{J}$, where $\bar{J} = \frac{1}{2}(J_1 + J_2)$ and $\bar{J}' = \frac{1}{8}(J'_1 + \dots + J'_8)$, shown as a function of q_b . The vertical lines indicate the maximum value of q_b estimated from our peak electric field and the horizontal line shows the time average, denoted $\langle \alpha \rangle$, of the interaction ratio at this driving field.

order triplet processes of the form

$$\begin{aligned}
 H_D = \sum_i & [\Delta J'_{12}(t_{1,i}^\dagger t_{2,i+x}^\dagger + t_{1,i}^\dagger t_{2,i+x}^\dagger) \\
 & + \Delta J'_{34}(t_{2,i}^\dagger t_{1,i+x}^\dagger + t_{2,i}^\dagger t_{1,i+x}^\dagger) \\
 & + \Delta J'_{56}(t_{1,i}^\dagger t_{2,i+y}^\dagger + t_{1,i}^\dagger t_{2,i+y}^\dagger) \\
 & + \Delta J'_{78}(t_{2,i}^\dagger t_{1,i+y}^\dagger + t_{2,i}^\dagger t_{1,i+y}^\dagger)] + \text{H.c.},
 \end{aligned} \quad (4)$$

where the full set of eight inequivalent J' bonds is shown in Fig. 12 of App. G. This may be contrasted with the explicit treatment for $\text{SrCu}_2(\text{BO}_3)_2$ at equilibrium in Ref. [38], where all of these bilinear triplon terms vanish. The first term in each bracket describes the propagation of existing triplon excitations between dimers, relieving their strict localization, although the high-frequency os-

cillation of $\Delta J'$ does not allow any quasi-static changes of the flat triplon bands.

The second term in Eq. (4) describes two-triplon creation on neighboring dimer pairs, i.e. the direct excitation of the TBS from the singlet quantum ground state ($|s\rangle$). While the triplon pairs are created initially on adjacent dimers, on the timescale of the spin system they will optimize their relative configuration to form the most strongly bound state [38], which is depicted very schematically on the right side of Fig. 2(a). Because lattice excitations cannot change the spin quantum numbers ($\Delta S_{\text{tot}} = 0$) in a spin-isotropic Hamiltonian, only transitions to the STTBS ($S = 0$) are allowed. The coefficients $\Delta J'_{12}, \dots, \Delta J'_{78}$ in Eq. (4) are a direct expression of the frustration-breaking, making fully explicit the origin of this phonon-driven triplon pair creation.

B. Lattice dynamics and density functional theory

We perform two types of quantitative calculation within this framework. To model the nonlinear effects of the driven phonons, we follow Refs. [35] and [60] by considering $H_D(q_m, q_n)$ as a dynamic perturbation through the coupling term $H_{\text{Em-Ph}}$ in Eq. (1). In our experiments (Sec. III), two different IR-active phonon modes show the strongest driving. Labelling these by a and b , their equations of motion are

$$\begin{aligned} \ddot{q}_a + \gamma_a \dot{q}_a + \omega_a^2 q_a &= -B_a E_{\text{THz}}(t), \\ \ddot{q}_b + \gamma_b \dot{q}_b + \omega_b^2 q_b &= -B_b E_{\text{THz}}(t), \end{aligned} \quad (5)$$

where $\omega_a = 3.80$ THz and $\omega_b = 4.60$ THz are the experimental phonon frequencies, $\gamma_a = 0.02$ THz and $\gamma_b = 0.03$ THz are their respective damping rates (App. B), and E_{THz} is the external THz driving field taken from experiment [Fig. 1(b)]. B_a and B_b are the dipolar coupling constants, which depend on the effective charges (Z_{eff}^i), the transmission coefficients (β_m), and the reduced masses of the phonon modes, which we deduce from the maximum displacements $\delta_a = 0.04$ Å and $\delta_b = 0.17$ Å calculated following App. A. From Eq. (5) we compute as a function of time the net atomic displacement due to the two leading phonon modes, $q_t = q_a + q_b$, obtaining the result shown in Fig. 5(c).

The second type of calculation is to compute the magnetic interaction parameters by DFT. These calculations were performed using the Quantum Espresso package [61], an open-source tool for electronic structure calculations based on DFT and the pseudopotential plane-wave technique. Exchange and correlation effects were modelled using the PBE functional [62], augmented by a Hubbard U term to include the strongly correlated nature of the Cu $3d$ electrons. The calculation of magnetic interactions is a self-consistent process in which the lattice structure is relaxed fully in a selected collinear spin configuration for each fixed value of the effective U parameter and then the total energies of the different magnetic configurations are compared [63] by mapping them onto the terms $H_0 + H_H$ in Eq. (3) to determine equilibrium values for J and J' [Eq. (2)]. The full details of this process and of its intrinsic accuracy are presented in App. G.

In the initial step of our calculations we used this procedure to refine U , deducing that $U = 11.4$ eV yields the magnetic interactions $J = 7.24$ meV (84.0 K) and $J' = 4.28$ meV (49.7 K), in good agreement with experimental findings [38] and giving a coupling ratio $\alpha = 0.592$ for the equilibrium lattice structure. We then extended these methods to estimate the phonon-induced modulation of the magnetic interaction parameters by computing the temporal evolution of the frustration-breaking terms, $\Delta J'(t)$. For this we evaluated the magnetic interactions in a dense sequence of different “frozen phonon” configurations of the lattice. Each atom in the $\text{SrCu}_2(\text{BO}_3)_2$ structure was displaced by $q_m \hat{u}_{im}$, where

q_m is the instantaneous displacement amplitude of excited phonon mode m , \hat{u}_{im} denotes the set of normal-mode vectors taken from Ref. [46], and we restricted our calculations to $m = a, b$ with $\omega_a = 3.80$ and $\omega_b = 4.60$ THz. The displacements of the atoms from equilibrium reduce the lattice symmetry, as represented in Fig. 5(a), and hence require more complex calculations of more interaction parameters in a larger unit cell, as detailed in App. G.

In Fig. 5(b) we show the four different interdimer interaction parameters (J'_1, J'_2, J'_3, J'_4) neighboring each vertical spin dimer as functions of the largest scalar phonon displacement amplitude, q_b , whose maximum value is δ_b . We stress that the parameters (J'_5, J'_6, J'_7, J'_8), which we do not show, are different from (J'_1, J'_2, J'_3, J'_4) for these specific members of the E -symmetric phonon doublets, but are interchanged with them for the other member of the doublet. Figure 5(b) shows that, while the phonon-induced variations in J_1 and J_2 are almost quadratic, the interactions $J'_{1,\dots,4}$ all have significant linear components. These result in large values of the frustration-breaking difference interactions, $\Delta J'$, well in excess of 10 K (i.e. reaching 20-30% of J' by this estimate).

To mimic our experiment, we superposed the phonon normal modes to obtain $q_t = q_a + q_b$ [Fig. 5(c)] at 285 time points in steps of 0.035 ps, in order to span 10 ps. The corresponding frustration-breaking interaction parameters, $\Delta J'_{12}$ and $\Delta J'_{34}$ [Fig. 5(d)], show a strong and in-phase oscillation controlled largely by q_b . In the frequency domain, this density of time steps reproduces well-resolved peaks at both the low frequency of the TBS peak and the intermediate frequency of the driven phonons. Even at the harmonic level we model, the IR phonons excited by the THz pump [Fig. 5(e)] create a nonlinear modulation of the interaction parameters [through Eq. (3)] with a rich spectrum [Fig. 5(f)]. This spectrum includes significant weight at the frequency $\omega_b - \omega_a$, whose resonance with the TBS [inset, Fig. 5(e)] ensures large values of the matrix element for two-triplon creation, $\langle \text{TBS} | \Delta J'(\omega) t_{1,i}^\dagger t_{2,j}^\dagger | s \rangle$, and hence the strong nonequilibrium population of this purely magnetic excitation that we report in Figs. 3(a) and 3(c).

V. DISCUSSION

Ideal frustration of magnetic interactions is the core attribute that leads quantum spin systems to form entirely unconventional and exotic phases, although some of the most fundamentally novel properties (such as fractional excitations, topological order, and entanglement) often remain largely hidden from conventional experimental probes. In this context, a static breaking of ideal frustration is often regarded as trivial, merely removing the properties that make the system special; in $\text{SrCu}_2(\text{BO}_3)_2$, a static $\Delta J'$ would restore triplon propagation, destabilize the bound states, and favor the nearby phase of long-ranged antiferromagnetic order [25]. However the

dynamical frustration-breaking we effect means that the static and equilibrium state of ideal frustration is retained, excluding most of these more trivial hallmarks and thereby offering an alternative route to the selective and controlled investigation of certain hidden properties.

While much has been made of “controlling quantum systems” on ultrafast timescales, we stress that ultrafast processes in magnetic materials have to date been restricted in large part to destroying, modulating the magnitude, or switching the direction of an ordered moment [10, 12, 16]. Here we have solved two further fundamental problems on the route to ultrafast dynamical control. The first is the coupling of light to a quantum magnet with no magnetic order. As a lattice-based route, magnetophononics achieves such coupling both universally, meaning for all forms of interaction in condensed matter – however “hidden” the resulting unconventional order may be, or how “forbidden” a process may be, in experiments performed at equilibrium – and in an intrinsically resonant manner. The second is the frequency-matching problem by which the light-driven pump (the phonons) can be tuned to the target (magnetic) excitations, and for this purpose our second-order nonlinear variant of magnetophononics allows a universal extension of lattice control to very low (phonon difference) and high (phonon sum) frequencies.

At the conceptual level, by periodic driving of a quantum system one may expect to achieve state control, population control, or spectral control, all of which are covered in the term “Floquet engineering” [6]. In the true Floquet regime, where the frequency of the light far exceeds the system frequencies, driving causes no significant modification of the basis states (very little energy is transferred), but induces phase-coherent superpositions of these states that can have dramatically different properties. When the light frequency resonates with a system transition, the high available laser intensities allow one to achieve strongly nonequilibrium state populations, raising the prospect of driving a nonequilibrium Bose condensation in suitable systems. While these processes may alter the spectrum of the system as a secondary effect, a direct modulation of the system parameters can be achieved in one of two ways. A simple situation would be the opposite limit to $\text{SrCu}_2(\text{BO}_3)_2$, where slow phonons in a material with high magnetic energies give linear control of the parameters. However, magnetophononic driving at the resonant frequencies of the spin system offers the clearest potential for unconventional dynamical phenomena, including qualitatively different types of hybrid spin-phonon state, engineering of the spin and phonon energies, and strong mutual feedback effects on state populations [64].

In $\text{SrCu}_2(\text{BO}_3)_2$ we have achieved control in the form of creating a significant nonequilibrium population of a target excited state. However, this population was not sufficient, at our available electric fields, to cause a detectable modification of the TBS energy. In the limit exemplified by $\text{SrCu}_2(\text{BO}_3)_2$, where the phonons are much

faster than the spin excitations and thus resonant driving is caused by a rather weak second-harmonic component, we have not yet been able to alter the TBS or triplon energies directly. However, considering the many different phonon normal modes and frequencies available in $\text{SrCu}_2(\text{BO}_3)_2$, it is clear that such dynamical driving presents a wide variety of highly specific control channels for different interactions in the atomic structure, in stark contrast to the universal alterations effected by conventional static control channels, such as an applied pressure or magnetic field. Here we recall also that the pulsed nature of the experimental driving, while essential for heat control in the sample, implies that all of the phenomena observed will be long-lived transients constituting an approximation to the true nonequilibrium states of the driven system.

As a more general route to nonresonant interaction control, Fig. 5(g) indicates for the example of a driven ω_b phonon how the method of driving IR-active phonons in the harmonic regime can cause a strong increase in the instantaneous ratio of the spatially averaged interactions, $\alpha = \bar{J}'/\bar{J}$. While recent experimental [43] and theoretical [44] studies have highlighted the role of the “pantograph” phonon [42] in modulating α , this A_1 -symmetric mode, found at 6.1 THz in Raman measurements, cannot be excited coherently in the same way as IR phonons. Because the phonons are so much faster than the magnetic interactions, the important quantity is the time average of $\alpha(q_b)$ in Fig. 5(g), whose rise with q_b indicates the prospect, at still higher electric fields, of a driven, dynamical approach to the static QPT into the plaquette phase of $\text{SrCu}_2(\text{BO}_3)_2$, i.e. with no frustration-breaking effects on long timescales. Although it represents the effect of only a single phonon, Fig. 5(g) suggests that the dynamical approach to controlling α is clearly comparable in range with hydrostatic pressure techniques [26, 31]; indeed our current studies, which were not optimized for this purpose, indicate a high potential for achieving significantly stronger static effects by further increasing the THz field strength and by tailoring of the excited phonon modes.

Beyond the primary superexchange interactions (J and J'), further terms in the modulated spin Hamiltonian can also produce spin excitations that are normally weak or forbidden. $\text{SrCu}_2(\text{BO}_3)_2$ has Dzyaloshinskii-Moriya (DM) interactions [36], which are small (3% of J), but are important in applied magnetic fields, including to create topological states [38]. The driving of symmetry-breaking IR phonons also creates dynamical antisymmetric spin interactions directly analogous to the modulation of J and J' . In $\text{SrCu}_2(\text{BO}_3)_2$, our experiments demonstrate no discernible role for driven DM interactions, because the one-triplon excitation process ($\Delta S_{\text{tot}} = 1$) at 0.71 THz should be excited by the same difference-frequency envelope as the TBS, but clearly no feature is visible above the detection threshold at this frequency in Fig. 3(c). More generally, however, one may use selective nonlinear IR phonon driving to manipulate both the

symmetric and antisymmetric magnetic interactions in systems such as skyrmion lattices and chiral spin liquids, where both couplings play an essential role.

In summary, we have demonstrated coherent light-driven spin dynamics in a purely quantum magnetic system. By the resonant excitation of phonons and their nonlinear mixing to span a very wide (sum and difference) frequency range, our experimental protocol meets the intrinsic challenge of spin-phonon frequency-matching. We have applied it to $\text{SrCu}_2(\text{BO}_3)_2$ and achieved the selective excitation of the singlet branch of the two-triplon bound state without exciting individual triplons. We have shown theoretically how this process occurs, once the driven phonons relieve the ideal magnetic frustration, and have performed DFT calculations to estimate the magnitude of the interaction modulation. Our results open an additional time dimension for exploring quantum magnetic phenomena that to date have been probed only by quasi-static stimuli, and because it uses the lattice as its medium our method is applicable without restriction to all the exotic spin states available in quantum magnetic materials. In view of ongoing tech-

nical progress at all the frontiers of narrow-band spectra, high intensities, and ultrashort pulses, one may anticipate order-of-magnitude improvements in both driving and detection that will place dynamically driven phenomena within reach in multiple classes of quantum material.

ACKNOWLEDGMENTS

We are grateful to C. Homes for sharing the calculated phonon eigenvectors. We thank T. Cea, M. Först, S. Furuya, A. Kimel, R. Mankowsky, F. Mila, A. Razpopov, G. S. Uhrig, and R. Valentí for valuable discussions. This research was supported by the European Research Council (ERC) within the EU Horizon 2020 research and innovation programme under Grant No. 681654 (HyperQC), by the MARVEL National Centre of Competence in Research of the Swiss National Science Foundation and by the DFG (German Research Foundation) through Grants No. UH90/13-1 and UH90/14-1.

-
- [1] P. Salén, M. Basini, S. Bonetti, J. Hebling, M. Krasnikov, A. Y. Nikitin, G. Shamuilov, Z. Tibai, V. Zhaunerchyk, and V. Goryashko, *Phys. Rep.* **836-837**, 1 (2019).
- [2] D. Nicoletti and A. Cavalleri, *Adv. Opt. Photon.* **8**, 401 (2016).
- [3] M. Mitrano, A. Cantaluppi, D. Nicoletti, S. Kaiser, A. Perucchi, S. Lupi, P. Di Pietro, D. Pontiroli, M. Riccò, S. R. Clark, D. Jaksch, and A. Cavalleri, *Nature* **530**, 461 (2016).
- [4] A. D. Caviglia, R. Scherwitsl, P. Popovich, W. Hu, H. Bromberger, R. Singla, M. Mitrano, M. C. Hoffmann, S. Kaiser, P. Zubko, S. Gariglio, J.-M. Triscone, M. Först, and A. Cavalleri, *Phys. Rev. Lett.* **108**, 136801 (2012).
- [5] T. Kubacka, J. A. Johnson, M. C. Hoffmann, C. Vicario, S. de Jong, P. Beaud, S. Grübel, S.-W. Huang, L. Huber, L. Patthey, Y.-D. Chuang, J. J. Turner, G. L. Dakovski, W.-S. Lee, M. P. Minitti, W. Schlotter, R. G. Moore, C. P. Hauri, S. M. Koochpayeh, V. Scagnoli, G. Ingold, S. L. Johnson, and U. Staub, *Science* **343**, 1333 (2014).
- [6] T. Oka and S. Kitamura, *Annu. Rev. Condens. Matter Phys.* **10**, 387 (2019).
- [7] D. N. Basov, R. D. Averitt, and D. Hsieh, *Nat. Mater.* **16**, 1077 (2017).
- [8] A. de la Torre, D. M. Kennes, M. Claassen, S. Gerber, J. W. McIver, and M. Sentef, *Rev. Mod. Phys.* **93**, 041002 (2021).
- [9] C. Vicario, C. Ruchert, F. Ardana-Lamas, P. M. Derlet, B. Tudu, J. Luning, and C. P. Hauri, *Nat. Photonics* **7**, 720 (2013).
- [10] T. Kampfrath, A. Sell, G. Klatt, A. Pashkin, S. Mährlein, T. Dekorsy, M. Wolf, M. Fiebig, A. Leitenstorfer, and R. Huber, *Nat. Photonics* **5**, 31 (2011).
- [11] R. Mikhaylovskiy, E. Hendry, A. Secchi, J. Mentink, M. Eckstein, A. Wu, R. Pisarev, V. Kruglyak, M. Katsnelson, T. Rasing, and A. Kimel, *Nat. Commun.* **6**, 8190 (2015).
- [12] M. Först, A. D. Caviglia, R. Scherwitsl, R. Mankowsky, P. Zubko, V. Khanna, H. Bromberger, S. B. Wilkins, Y.-D. Chuang, W. S. Lee, W. F. Schlotter, J. J. Turner, G. L. Dakovski, M. P. Minitti, J. Robinson, S. R. Clark, D. Jaksch, J.-M. Triscone, J. P. Hill, S. S. Dhesi, and A. Cavalleri, *Nat. Mater.* **14**, 883 (2015).
- [13] T. F. Nova, A. Cartella, A. Cantaluppi, M. Först, D. Bossini, R. V. Mikhaylovskiy, A. V. Kimel, R. Merlin, and A. Cavalleri, *Nat. Phys.* **13**, 132 (2017).
- [14] M. Fechner, A. Sukhov, L. Chotorlishvili, C. Kenel, J. Berakdar, and N. A. Spaldin, *Phys. Rev. Mater.* **2**, 064401 (2018).
- [15] D. Afanasiev, J. R. Hortensius, B. A. Ivanov, A. Sasani, E. Bousquet, Y. M. Blanter, R. V. Mikhaylovskiy, A. V. Kimel, and A. D. Caviglia, *Nat. Mater.* **20**, 607 (2021).
- [16] A. S. Disa, M. Fechner, T. F. Nova, B. Liu, M. Först, D. Prabhakaran, P. G. Radaelli, and A. Cavalleri, *Nat. Phys.* **16**, 937 (2020).
- [17] A. Kirilyuk, A. V. Kimel, and T. Rasing, *Rev. Mod. Phys.* **82**, 2731 (2010).
- [18] P. Němec, M. Fiebig, T. Kampfrath, and A. V. Kimel, *Nat. Phys.* **14**, 229 (2018).
- [19] S. Sachdev, *Nat. Phys.* **4**, 173 (2008).
- [20] L. Savary and L. Balents, *Rep. Prog. Phys.* **80**, 016502 (2016).
- [21] C. Broholm, R. J. Cava, S. A. Kivelson, D. G. Nocera, M. R. Norman, and T. Senthil, *Science* **367** (2020).
- [22] S. Miyahara and K. Ueda, *J. Phys. Condens. Matter* **15**, R327 (2003).
- [23] P. W. Anderson, *Mat. Res. Bull.* **8**, 153 (1973).
- [24] B. Sriram Shastry and B. Sutherland, *Physica B+C* **108**, 1069 (1981).
- [25] P. Corboz and F. Mila, *Phys. Rev. B* **87**, 115144 (2013).
- [26] M. E. Zayed, C. Rüegg, J. Larrea J., A. M. Läuchli,

- C. Panagopoulos, S. S. Saxena, M. Ellerby, D. F. McMorrow, T. Strässle, S. Klotz, G. Hamel, R. A. Sadykov, V. Pomjakushin, M. Boehm, M. Jiménez-Ruiz, A. Schneidewind, E. Pomjakushina, M. Stingaciu, K. Conder, and H. M. Rønnow, *Nat. Phys.* **13**, 962 (2017).
- [27] J. Guo, G. Sun, B. Zhao, L. Wang, W. Hong, V. A. Sidorov, N. Ma, Q. Wu, S. Li, Z. Y. Meng, A. W. Sandvik, and L. Sun, *Phys. Rev. Lett.* **124**, 206602 (2020).
- [28] J. Larrea Jiménez, S. P. G. Crone, E. Fogh, M. E. Zayed, R. Lortz, E. Pomjakushina, K. Conder, A. M. Läuchli, L. Weber, S. Wessel, A. Honecker, B. Normand, C. Rüegg, P. Corboz, H. M. Rønnow, and F. Mila, *Nature* **592**, 370 (2021).
- [29] H. Kageyama, K. Yoshimura, R. Stern, N. V. Mushnikov, K. Onizuka, M. Kato, K. Kosuge, C. P. Slichter, T. Goto, and Y. Ueda, *Phys. Rev. Lett.* **82**, 3168 (1999).
- [30] M. Takigawa, M. Horvatić, T. Waki, S. Krämer, C. Berthier, F. Lévy-Bertrand, I. Sheikin, H. Kageyama, Y. Ueda, and F. Mila, *Phys. Rev. Lett.* **110**, 067210 (2013).
- [31] S. Haravifard, D. Graf, A. E. Feiguin, C. D. Batista, J. C. Lang, D. M. Silevitch, G. Srajer, B. D. Gaulin, H. A. Dabkowska, and T. F. Rosenbaum, *Nat. Commun.* **7**, 11956 (2016).
- [32] C. Rüegg, B. Normand, M. Matsumoto, A. Furrer, D. F. McMorrow, K. W. Krämer, H. U. Güdel, S. N. Gvasaliya, H. Mutka, and M. Boehm, *Phys. Rev. Lett.* **100**, 205701 (2008).
- [33] P. Merchant, B. Normand, K. W. Krämer, M. Boehm, D. F. McMorrow, and C. Rüegg, *Nat. Phys.* **10**, 373 (2014).
- [34] M. Uhlarz, C. Pfeleiderer, and S. M. Hayden, *Phys. Rev. Lett.* **93**, 256404 (2004).
- [35] M. Först, C. Manzoni, S. Kaiser, Y. Tomioka, Y. Tokura, R. Merlin, and A. Cavalleri, *Nat. Phys.* **7**, 854 (2011).
- [36] H. Nojiri, H. Kageyama, Y. Ueda, and M. Motokawa, *J. Phys. Soc. Jpn.* **72**, 3243 (2003).
- [37] B. D. Gaulin, S. H. Lee, S. Haravifard, J. P. Castellán, A. J. Berlinsky, H. A. Dabkowska, Y. Qiu, and J. R. D. Copley, *Phys. Rev. Lett.* **93**, 267202 (2004).
- [38] P. A. McClarty, F. Krüger, T. Guidi, S. F. Parker, K. Refson, A. W. Parker, D. Prabhakaran, and R. Coldea, *Nat. Phys.* **13**, 736 (2017).
- [39] P. Lemmens, M. Grove, M. Fischer, G. Güntherodt, V. N. Kotov, H. Kageyama, K. Onizuka, and Y. Ueda, *Phys. Rev. Lett.* **85**, 2605 (2000).
- [40] A. Gozar, B. S. Dennis, H. Kageyama, and G. Blumberg, *Phys. Rev. B* **72**, 064405 (2005).
- [41] T. Rõõm, U. Nagel, E. Lippmaa, H. Kageyama, K. Onizuka, and Y. Ueda, *Phys. Rev. B* **61**, 14342 (2000).
- [42] G. Radtke, A. Saúl, H. A. Dabkowska, M. B. Salamon, and M. Jaime, *Proc. Natl. Acad. Sci.* **112**, 1971 (2015).
- [43] S. Bettler, L. Stoppel, Z. Yan, S. Gvasaliya, and A. Zheleudev, *Phys. Rev. Res.* **2**, 012010 (2020).
- [44] D. I. Badrtdinov, A. A. Tsirlin, V. V. Mazurenko, and F. Mila, *Phys. Rev. B* **101**, 224424 (2020).
- [45] C. Vicario, A. Trisorio, S. Allenspach, C. Rüegg, and F. Giorgianni, *Appl. Phys. Lett.* **117**, 101101 (2020).
- [46] C. C. Homes, S. V. Dordevic, A. Gozar, G. Blumberg, T. Rõõm, D. Hüvonen, U. Nagel, A. D. LaForge, D. N. Basov, and H. Kageyama, *Phys. Rev. B* **79**, 125101 (2009).
- [47] B. Liu, H. Bromberger, A. Cartella, T. Gebert, M. Först, and A. Cavalleri, *Opt. Lett.* **42**, 129 (2017).
- [48] M. B. Agranat, O. V. Chefonov, A. V. Ovchinnikov, S. I. Ashitkov, V. E. Fortov, and P. S. Kondratenko, *Phys. Rev. Lett.* **120**, 085704 (2018).
- [49] M. E. Zayed, C. Rüegg, T. Strässle, U. Stuhr, B. Roessli, M. Ay, J. Mesot, P. Link, E. Pomjakushina, M. Stingaciu, K. Conder, and H. M. Rønnow, *Phys. Rev. Lett.* **113**, 067201 (2014).
- [50] A. Wietek, P. Corboz, S. Wessel, B. Normand, F. Mila, and A. Honecker, *Phys. Rev. Res.* **1**, 033038 (2019).
- [51] S. Schlauderer, C. Lange, S. Baierl, T. Ebnet, C. P. Schmid, D. C. Valovcin, A. K. Zvezdin, A. V. Kimel, R. V. Mikhaylovskiy, and R. Huber, *Nature* **569**, 383 (2019).
- [52] H. J. Zeiger, J. Vidal, T. K. Cheng, E. P. Ippen, G. Dresselhaus, and M. S. Dresselhaus, *Phys. Rev. B* **45**, 768 (1992).
- [53] G. Jnawali, D. Boschetto, L. M. Malard, T. F. Heinz, G. Sciaini, F. Thiemann, T. Payer, L. Kremeyer, F.-J. M. zu Heringdorf, and M. H. von Hoegen, *Appl. Phys. Lett.* **119**, 091601 (2021).
- [54] F. Giorgianni, M. Udina, T. Cea, E. Paris, M. Caputo, M. Radovic, L. Boie, J. Sakai, C. W. Schneider, and S. L. Johnson, *Commun. Phys.* **5**, 103 (2022).
- [55] H. Yamakawa, T. Miyamoto, T. Morimoto, T. Terashige, H. Yada, N. Kida, M. Suda, H. M. Yamamoto, R. Kato, K. Miyagawa, K. Kanoda, and H. Okamoto, *Nat. Mater.* **16**, 1100 (2017).
- [56] A. T. Tarekegne, H. Hirori, K. Tanaka, K. Iwaszczuk, and P. U. Jepsen, *New J. Phys.* **19**, 123018 (2017).
- [57] S. Hubmann, G. V. Budkin, M. Urban, V. V. Bel'kov, A. P. Dmitriev, J. Ziegler, D. A. Kozlov, N. N. Mikhailov, S. A. Dvoretzky, Z. D. Kvon, D. Weiss, and S. D. Ganichev, *J. Infrared, Millimeter, and Terahertz Waves* **41**, 1155 (2020).
- [58] M. Kozina, M. Fechner, P. Marsik, T. van Driel, J. M. Glowina, C. Bernhard, M. Radovic, D. Zhu, S. Bonetti, U. Staub, and M. C. Hoffmann, *Nat. Phys.* **15**, 387 (2019).
- [59] B. Normand and C. Rüegg, *Phys. Rev. B* **83**, 054415 (2011).
- [60] A. A. Melnikov, K. N. Boldyrev, Y. G. Selivanov, V. P. Martovitskii, S. V. Chekalin, and E. A. Ryabov, *Phys. Rev. B* **97**, 214304 (2018).
- [61] P. Giannozzi, O. Andreussi, T. Brumme, O. Bunau, M. B. Nardelli, M. Calandra, R. Car, C. Cavazzoni, D. Ceresoli, M. Cococcioni, N. Colonna, I. Carnimeo, A. D. Corso, S. de Gironcoli, P. Delugas, R. A. DiStasio, A. Ferretti, A. Floris, G. Fratesi, G. Fugallo, R. Gebauer, U. Gerstmann, F. Giustino, T. Gorni, J. Jia, M. Kawamura, H.-Y. Ko, A. Kokalj, E. Küçükbenli, M. Lazzeri, M. Marsili, N. Marzari, F. Mauri, N. L. Nguyen, H.-V. Nguyen, A. Otero de la Roza, L. Paulatto, S. Poncé, D. Rocca, R. Sabatini, B. Santra, M. Schlipf, A. P. Seitsonen, A. Smogunov, I. Timrov, T. Thonhauser, P. Umari, N. Vast, X. Wu, and S. Baroni, *J. Phys. Condens. Matter* **29**, 465901 (2017).
- [62] J. P. Perdew, K. Burke, and M. Ernzerhof, *Phys. Rev. Lett.* **77**, 3865 (1996).
- [63] G. Radtke, A. Saúl, H. A. Dabkowska, B. D. Gaulin, and G. A. Botton, *Phys. Rev. B* **77**, 125130 (2008).
- [64] M. Yarmohammadi, M. Krebs, G. S. Uhrig, and B. Normand, arXiv:2303.00125.

- [65] F. Giorgianni, J. Sakai, and S. Lupi, *Nat. Commun.* **10**, 1159 (2019).
- [66] H. G. Roskos, M. D. Thomson, M. Kieß, and T. Löffler, *Laser & Photonics Rev.* **1**, 349 (2007).
- [67] D. M. Juraschek and S. F. Maehrlein, *Phys. Rev. B* **97**, 174302 (2018).
- [68] D. S. Sivia and J. Skilling, *Data Analysis - A Bayesian Tutorial*, 2nd ed. (Oxford University Press, 2006).
- [69] T. Kampfrath, K. Tanaka, and K. A. Nelson, *Nat. Photonics* **7**, 680 (2013).
- [70] A. N. Vasil'ev, M. M. Markina, A. V. Inyushkin, and H. Kageyama, *JETP Lett.* **73**, 633 (2001).
- [71] G. Prandini, A. Marrazzo, I. E. Castelli, N. Mounet, and N. Marzari, *npj Comput. Mater.* **4**, 72 (2018).
- [72] G. Prandini, A. Marrazzo, I. E. Castelli, N. Mounet, and N. Marzari, *Mater. Cloud Arch.*, 2018.0001/v4 (2020).
- [73] C. Vecchini, O. Adamopoulos, L. C. Chapon, A. Lappas, H. Kageyama, Y. Ueda, and A. Zorko, *J. Solid State Chem.* **182**, 3275 (2009).

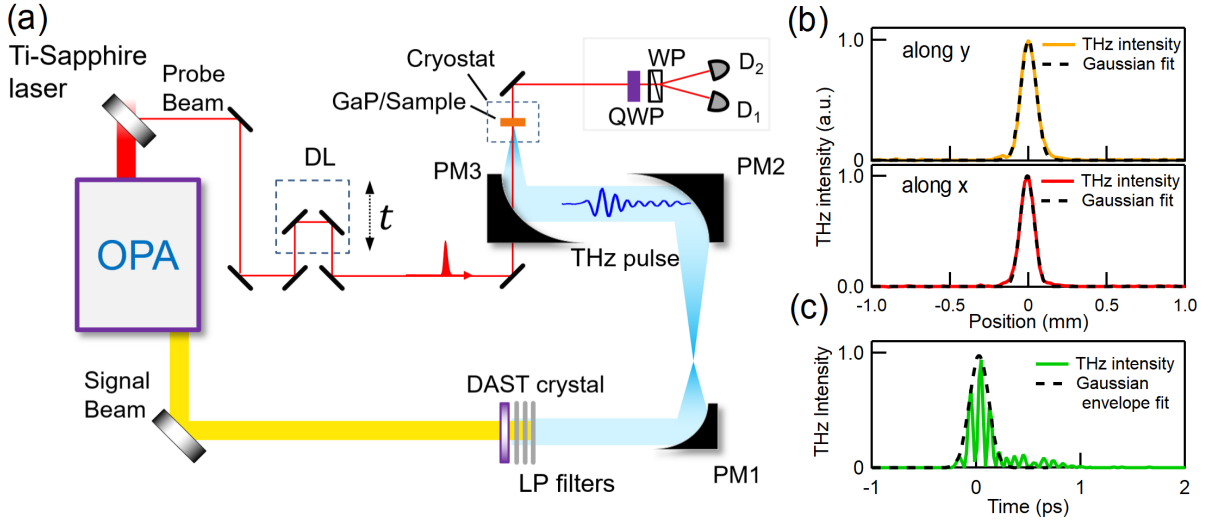


FIG. 6. **Experimental THz-pump, optical-probe set-up and measured THz pump parameters.** (a) Schematic representation showing the Optical Parametric Amplifier (OPA), parabolic mirrors (PM1-PM3), delay line (DL), quarter-wave plate (QWP), Wollaston prism (WP), and detectors (D1-D2). (b) THz beam profile at the sample position measured by the THz camera. Beam waists obtained by Gaussian fitting are respectively $w_x = 88 \mu\text{m}$ and $w_y = 96 \mu\text{m}$ (average waist $w = 92 \mu\text{m}$). (c) Temporal THz intensity waveform obtained as the square of the electric field measured by electro-optic sampling, using a Gaussian-envelope fit to determine the pulse duration.

Appendix A: Experiment

Single crystals of $\text{SrCu}_2(\text{BO}_3)_2$ were grown using an optical floating-zone furnace (FZ-T-10000-H-IV-VP-PC, Crystal System Corp., Japan) with four 300 W halogen lamps as the heat source. The growth rate was 0.25 mm/h, with both feeding and seeding rods being rotated at approximately 15 rpm in opposite directions to ensure the homogeneity of the liquid; an argon atmosphere with 20% oxygen was maintained at 5 bar during growth. The high structural quality and orientation of the resulting single crystal were confirmed by x-ray diffraction and the high magnetic quality (absence of impurities) by susceptibility measurements. The crystal was cut using a diamond wire saw and cleaved along the $a'b'$ -plane to give a sample of dimensions $1 \times 3 \times 0.24 \text{ mm}^3$ that was used for

the experiments.

The THz-pump and optical-probe set-up is shown in Fig. 6(a) [45]. The output of a 20 mJ, 55 fs, 800 nm Ti:sapphire laser was used to drive an optical parametric amplifier (OPA), which provides ultrashort, multi-mJ pulses [65]. Single-cycle THz pulses were generated by optical rectification, using a crystal of DAST (4-N,N-dimethylamino-4'-N'-methyl-stilbazolium tosylate, from Rainbow Photonics), of the OPA signal at $1.5 \mu\text{m}$. The OPA pulse energy of 3.2 mJ gave an NIR pump fluence at the crystal surface of approximately 5 mJcm^{-2} . Three low-pass filters, two with a 20 THz cut-off frequency and one with 10 THz, were used after the THz generation step to block the residual OPA beam, and gave an extinction ratio for the pump in excess of 105. For the pump pulses, an additional high-pass filter with a cut-

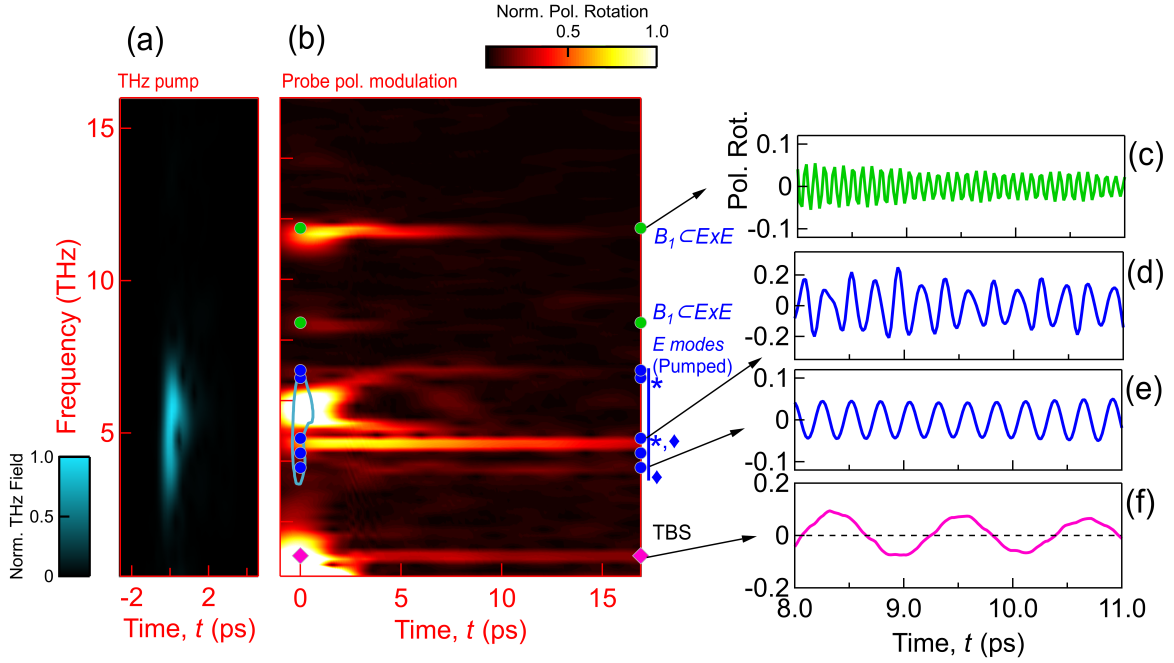


FIG. 7. **Time-frequency THz-driven dynamics.** (a) THz pump electric-field amplitude. (b) Pump-induced polarization modulation in $\text{SrCu}_2(\text{BO}_3)_2$ at 4 K. In panel (a), the color contours around $t = 0$ are based on the FWHM isoline of the amplitude. In panel (b), the blue circles indicate the frequencies of the E -symmetric IR-active phonon modes that are pumped directly, where our measured values of 3.80, 4.27, 6.75, and 7.00 THz match within the experimental error with those of Ref. [46], whereas the 4.60 THz mode we measure is tabulated there as 4.75 THz. Green circles show the frequencies of B_1 -symmetric modes at 8.57 THz and 11.7 THz [46] that are not IR-active but are excited by sum-frequency processes, which are expected to involve respectively the E -symmetric modes indicated with diamonds (3.80 THz and 4.60 THz) and with asterisks (4.60 THz and 7.00 THz). The pink diamond marks the frequency of the TBS, $\omega_{\text{TBS}} = 0.87$ THz (taken from Refs. [39, 40]); this mode is not electromagnetically active and is driven by the nonlinear (difference-frequency) spin-phonon coupling discussed in Sec. IV. (c-f) Temporal dynamics, obtained by numerical band-pass filters, of the normalized polarization rotations measured for some of the primary excited modes.

off of 4.2 THz was used to drive the primary IR-active phonons while ensuring a negligible spectral weight at the frequency of the leading magnetic modes [Fig. 3(a)]. To select the four different pump pulses shown in Fig. 4(c), we used respectively a 2 THz low-pass filter, a 3 THz band-pass filter, a 4.2 THz high-pass filter coupled with a 6 THz low-pass filter, and a 6 THz band-pass filter.

For the measurement of properties dependent on the pump strength, the THz electric field was tuned by three wire-grid polarizers. Peak electric fields were reached by tight focusing of the THz beam using three parabolic mirrors [65]. To estimate the electric-field strength of the pump pulses shown in Fig. 1, we apply the formula [66]

$$E_{\text{THz}} = \sqrt{\frac{z_0 E_p^4 \sqrt{\ln 2}}{\pi \sqrt{\pi} w^2 \tau_{\text{FWHM}}}}, \quad (\text{A1})$$

where z_0 is the vacuum impedance and we measured (i) the THz energy per pulse, $E_p = 0.8 \mu\text{J}$, using a calibrated THz energymeter (Gentec THZ12D3S-VP-D0); (ii) the beam waist, $w = 92 \mu\text{m}$, obtained by a Gaussian fit of

the beam profile [Fig. 6(b)], which was measured with a micro-bolometric THz camera (NEC IRV-T0830); (iii) the pulse duration, $\tau_{\text{FWHM}} = 0.21$ ps, obtained from the FWHM of the Gaussian envelope fitting the temporal intensity waveform of the THz pump [Fig. 6(c)], which was taken as the square of the electric field measured at the sample position by electro-optic sampling in a 200 μm -thick (110) GaP crystal with a 50 fs, 800 nm gating pulse obtained as a fraction of the Ti:sapphire beam. Our estimated electric-field strength, $E_{\text{THz}} = 3.2 \text{ MVcm}^{-1}$, is similar to other values in recent literature [47, 48].

The gating pulse was used to probe the ultrafast pump-induced polarization dynamics of the sample, which were measured by splitting the probe beam into two orthogonal components with a Wollaston prism. The THz electric field of the pump was polarized in the sample plane along the direction perpendicular to the optical table. The polarization of the probe relative to the sample was offset by 45° from the pump polarization. All measurements were performed in a He cryostat, which allowed a minimum sample temperature of 3.5 K to be reached.

For a quantitative analysis of the effect of E_{THz} on the

sample, the peak polarization, P_m , induced by the THz pulse resonant with a generic phonon mode, m , is [3]

$$P_m = \frac{\sigma_1(\omega_m)}{\omega_m} \tilde{E}_{\text{THz}}, \quad (\text{A2})$$

where ω_m is the angular frequency and $\sigma_1(\omega_m)$ the optical conductivity of the driven phonon. The polarization arises from the modulation of the dipole moment of the crystal, $P_m = n_d \delta_m \mu_m$, where $\mu_m = e |\sum_{im} \hat{u}_{im} Z_{\text{eff}}^i|$ is the magnitude of the charge displacement due to phonon mode m , \hat{u}_{im} is the normalized vector of displacements of each atom, i , in phonon mode m , Z_{eff}^i are the Born effective charges of each atom, n_d is the number of dipoles per unit volume, and δ_m is the maximum displacement coordinate of the phonon. The driving field, $\tilde{E}_{\text{THz}} = \beta_m E_{\text{THz}}$ in Eq. (A2), is the effective electric field inside the sample acting on the phonon [66], where $\beta_m = 1 - R_m$ is determined by the reflectivity at frequency ω_m .

To illustrate the estimation of the δ_m values induced by the THz electric field, we take the example of the 4.60 THz phonon mode, which is the strongest single feature of the driven response (Fig. 3) and is labelled $m = b$ in Sec. IV. Thus we use $\omega_b = 2\pi 4.6 \times 10^{12} \text{ s}^{-1}$, $\sigma_1(\omega_b) = 137 \text{ } \Omega^{-1} \text{ cm}^{-1}$ from Ref. [46], $n_d = V^{-1}$ with $V = 5.71 \times 10^{-22} \text{ cm}^{-3}$ the volume of the unit cell, and the value $\mu_b = 0.6e$ taken from our DFT calculations (below). The bandwidth of the external THz field, approximately 2.7 THz FWHM [Fig. 3(a)], is large compared to the linewidth of the phonon mode [0.1 THz FWHM, Fig. 4(c)], and by accounting for the reflection of the external field [Fig. 4(c)] we estimate $\beta_b \simeq 0.02$. Thus we deduce a maximum displacement of $\delta_b = 0.17 \text{ \AA}$, which is comparable to that estimated in SrTiO₃ [58].

Appendix B: Time-frequency analysis of THz-driven dynamics and mode symmetries

Figure 7 reports the temporal profile and frequency content measured for the THz pump pulse [Fig. 7(a)] and the resulting polarization rotations induced in the SrCu₂(BO₃)₂ sample at 4 K [Fig. 7(b)]. The spectral decomposition was computed using a Hamming sliding-window fast Fourier transform. It is clear that the distribution of frequencies in the THz pump pulse [Fig. 7(a)] causes not only a direct resonant driving of E -symmetric, IR-active phonons but also a less direct, nonlinear driving of B_1 -symmetric, Raman-active phonons at higher frequencies [Figs. 7(b-c)]; for this the low-temperature point group, D_{2d} (space group $\bar{1}42m$), permits the excitation of B_1 ($\subset E \times E$) phonons by the composition of two E -symmetric phonons. Similarly, the magnetic excitation from the singlet ground state to the TBS mode can be interpreted as a resonance driven by the difference-frequency harmonic components of the E -symmetric phonons shown in Figs. 7(d-e). The TBS [Fig. 7(f)] also has B_1 symmetry, as determined by Raman spectroscopy [39, 40], indicating that its driving re-

lies on the same symmetry composition ($B_1 \subset E \times E$). We comment that, because both the singlet ground state and the TBS are nonmagnetic ($S = 0$), the origin of the polarization rotation measured in SrCu₂(BO₃)₂ must lie in lattice (birefringence) effects, which are clearly enhanced by the spin-lattice coupling.

Appendix C: THz-driven nonlinear phonon dynamics

Our results (Sec. III) demonstrate that the resonant dynamic distortion of the lattice in response to intense and coherent THz excitation creates nonlinear channels for the transfer of energy to both magnetic and phononic modes. The phenomenon of sum-frequency ionic Raman scattering has been investigated recently in both experiment [35, 60] and theory [67], and our results include its clearest observation to date. To describe the driven nonlinear lattice dynamics that we observe, we consider two IR-active phonons with normal coordinates q_b and q_c , with corresponding frequencies ω_b and ω_c , and a Raman-active phonon with coordinate q_R and frequency ω_R . By discarding terms quadratic in q_R , on the assumption that the amplitude of the Raman mode will be much smaller than that of the IR modes driven by the THz pump ($|q_{b,c}| \gg |q_R|$), the minimal lattice potential to cubic order (i.e. lowest anharmonic order) is

$$V(q_b, q_c, q_R) = \frac{1}{2} \omega_b^2 q_b^2 + \frac{1}{2} \omega_c^2 q_c^2 + \frac{1}{2} \omega_R^2 q_R^2 + [c_{bb,R} q_b^2 + c_{bc,R} q_b q_c + c_{cc,R} q_c^2] q_R, \quad (\text{C1})$$

where the c coefficients specify the leading nonlinear coupling terms between the IR and Raman phonons. The equation of motion for a generic THz-driven, IR-active phonon mode, m , takes the form

$$\ddot{q}_m + \gamma_m \dot{q}_m = - \frac{\partial [V - B_m q_m E_{\text{THz}}(t)]}{\partial q_m}, \quad (\text{C2})$$

with γ_m the damping rate and B_m the dipole coupling constant introduced in Eq. (5). For a phonon that is Raman-active but not IR-active, the driving term is only $\partial V / \partial q_R$. The coherent THz-driven lattice dynamics are then described in the time domain from Eq. (C2), to leading order in q_R , by the coupled differential equations

$$\ddot{q}_b + \gamma_b \dot{q}_b + \omega_b^2 q_b = -B_b E_{\text{THz}}(t), \quad (\text{C3})$$

$$\ddot{q}_c + \gamma_c \dot{q}_c + \omega_c^2 q_c = -B_c E_{\text{THz}}(t), \quad (\text{C4})$$

$$\ddot{q}_R + \gamma_R \dot{q}_R + \omega_R^2 q_R = -[c_{bb,R} q_b^2 + c_{bc,R} q_b q_c + c_{cc,R} q_c^2]. \quad (\text{C5})$$

Clearly Eq. (C5) for the Raman phonon describes a damped harmonic oscillator driven by terms quadratic in the IR-active phonon displacements, resulting in sum-frequency excitation processes. The effectiveness of this driving then depends on the proximity of the combinations $2\omega_b$, $2\omega_c$, and $\omega_b + \omega_c$ (and indeed $\omega_c - \omega_b$) to ω_R .

The clearest example in Fig. 7(b) is the B_1 Raman mode with frequency $\omega_R = 11.7 \text{ THz}$ and damping

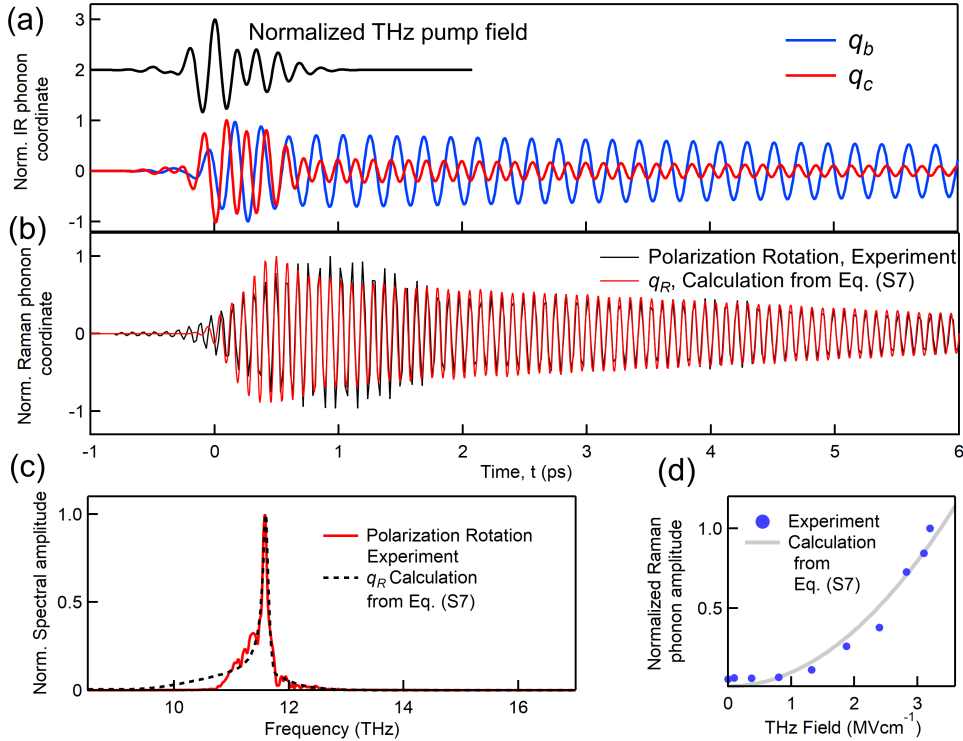


FIG. 8. **Sum-frequency ionic Raman excitation: experimental evidence and model.** (a) Normalized experimental THz driving field (black) and normalized time-dependent THz-driven atomic displacements, calculated from Eqs. (C3) and (C4), of the IR-active phonon modes q_b at $\omega_b = 4.60$ THz (blue) and q_c at $\omega_c = 7.0$ THz (red). (b) Time-dependent phonon-driven atomic displacement, q_R , of the Raman-active phonon mode, obtained from Eq. (C5) and compared to the normalized polarization rotation (Fig. 7) measured by using a numerical band-pass filter to remove the components of the lower-frequency modes. (c) Fourier-transformed amplitude of q_R and of the polarization rotation shown in panel (b). (d) Measured amplitude of q_R compared with the quadratic electric-field dependence given by Eq. (C5).

$\gamma_R = 0.2$ THz [Fig. 7(c)]. The two THz-pumped E -symmetric phonons marked by the asterisks have parameters $\omega_b = 4.60$ THz, $\gamma_b = 0.03$ THz and $\omega_c = 7.00$ THz, $\gamma_c = 0.10$ THz. Figure 8(a) shows the temporal evolution of q_b and q_c calculated from Eqs. (C3-C5) using the experimental THz pump field. As expected from the respective phonon frequencies, the Raman coordinate, q_R , is dominated by coherent oscillations at frequency $\omega_b + \omega_c$ [Fig. 8(b)], confirming the sum-frequency ionic Raman mechanism. The phenomenon is equally clear in the frequency domain, where the Fourier amplitudes of the measured and calculated dynamics are compared in Fig. 8(c). Because the amplitude of q_R varies linearly with each individual amplitude q_b or q_c [Eq. (C5)], it should scale quadratically with the THz field strength, as Fig. 8(d) confirms. We note again that all the phonon frequencies used in our analysis are the experimental values obtained from our pump-probe measurement, which with one exception match the FTIR spectroscopy measurements of Ref. [46] to within the experimental uncertainties; as a result of this match, we took all the phonon damping parameters (γ_m) from Ref. [46]. The exception was the phonon frequency $\omega_b = 4.60$ THz, found at 4.75 THz

by FTIR spectroscopy, where our measured value gave a significantly better account of the B_1 Raman frequency we observed at 11.58 THz. A similar analysis can be performed for the B_1 phonon mode at 8.57 THz, with driving by ω_b combined with the IR-active phonon at $\omega_a = 3.80$ THz [both marked by blue diamonds in Fig. 7(b)].

Appendix D: Fitting of phonon and TBS modes

The amplitudes of the ω_a and ω_b phonon modes shown in Fig. 4(a), and of the TBS mode shown in Fig. 4(b), were determined together with their uncertainties by a Gaussian fitting procedure in the frequency domain. Figure 9 shows the spectral peaks of the TBS mode, and of the two phonon modes, for a range of values of the peak electric field of the THz pump pulse, with the Gaussian fits shown as dashed black lines. In fitting a Gaussian function, $\mathcal{G}(a, \omega_0, w)$, to these peaks, the only free parameter was the peak amplitude, a , whereas the center frequency, ω_0 , and the Gaussian width, w , were fixed for every peak. The amplitudes and their uncertainties were then determined by the least-squares Gaussian fit

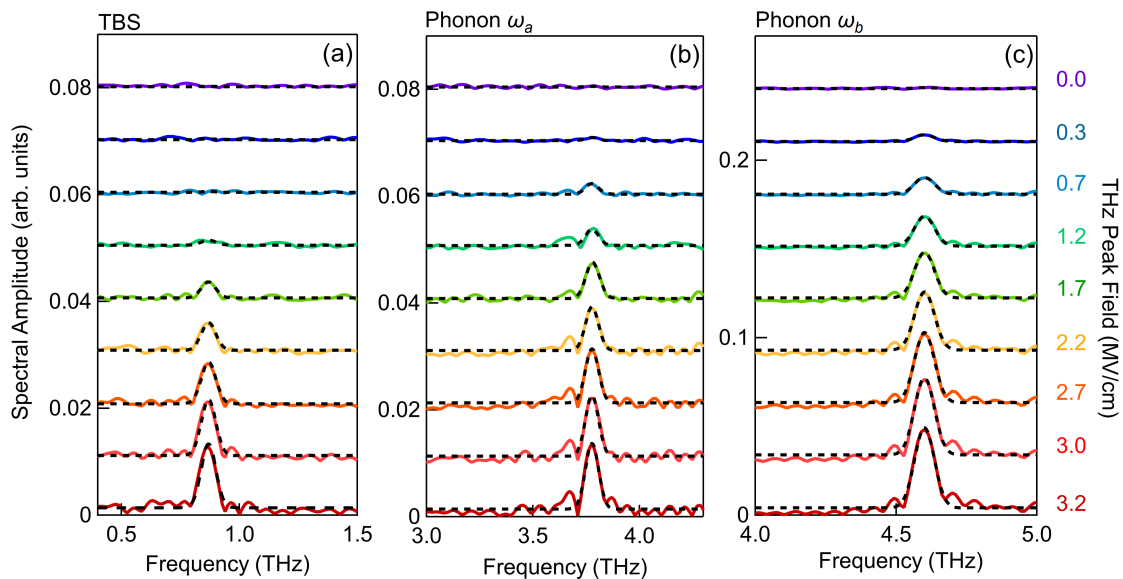


FIG. 9. **Extraction of mode amplitudes.** Spectral amplitude computed for the interval $1.9 \leq t \leq 14.4$ ps and shown for a range of THz pump field strengths with an added vertical offset. (a) TBS. (b) Phonon ω_a . (c) Phonon ω_b . Short-dashed black lines show fits to a Gaussian function, $\mathcal{G}(a, \omega_0, w)$, with the amplitude a as a free parameter. The center frequency (ω_0) and Gaussian width (standard deviation, w) parameters for the TBS are $\omega_0 = 0.87$ THz and $w = 0.06$ THz, for phonon mode a are $\omega_0 = 3.77$ THz and $w = 0.06$ THz, and for phonon mode b are $\omega_0 = 4.60$ THz and $w = 0.07$ THz.

method [68].

The nonlinear dependence of the TBS amplitude on the THz electric-field strength can be also be read from Fig. 9(a), by comparing it with the linear dependence of ω_a in Fig. 9(b). Both modes have comparable amplitudes at the maximum THz electric field, making clear the much faster decrease in the TBS amplitude at lower field strengths.

Appendix E: Dependence on polarity of the THz pump field

As Fig. 4(b) shows, the amplitude of the phonon-driven TBS excitation is proportional to the square of the driving electric field of the THz pump pulse. A further important test of our observations and modelling is therefore to invert the polarity of this field, as represented in Fig. 10(a). To implement this sign-inversion experimentally, we rotate the crystal for THz generation by 180° and compare the driven dynamics of the polarization-rotation signals. The results in the time domain are shown in Figs. 10(b-e). Because the E -symmetric (IR-active) phonon modes are excited directly, the carrier-envelope phase of the THz pump is imprinted onto them and Figs. 10(c-d) confirm a phase shift of 180° .

By contrast, the dynamics of the TBS [Fig. 10(b)] are invariant on changing the electric-field polarity, fully consistent with a quadratic driving mechanism. The dynamics of the Raman-active phonon at 11.6 THz, presented in App. C, are similarly insensitive to the change of polar-

ity [Fig. 10(e)], as expected of a sum-frequency process. We note that perfect inversion of the IR phonon signals, and perfect overlap of the TBS and Raman phonon signals, are actually obtained for a time shift of -20 fs in the $E^{(-)}$ signal. This can be attributed to the fact that rotation of the THz generation crystal may produce a small time-delay in the event of an inhomogeneity in its thickness (20 fs corresponds to approximately $6 \mu\text{m}$ in vacuum).

Appendix F: THz-pumped NIR transmission modulation

To demonstrate that ultrafast electronic processes, such as the displacive excitation of phonons [52], are not involved in the THz generation mechanism of the coherent phonons and TBS modes we observe, we have performed THz-pump, NIR-probe spectroscopy to measure the transient transmission modulation, $\Delta T/T$. Working under the same experimental conditions as for the measurements in Fig. 1(c), we measured the THz-induced NIR $\Delta T/T$ at a photon energy of 1.55 eV and show the results as a function of the pump-probe time delay in Fig. 11. The transient transmission can monitor the presence of ultrafast THz-induced carrier generation, which would appear as a peak at very short times, but the observed dynamics show no signature of such processes. Instead the $\Delta T/T$ dynamics show only a slow decrease of the sample transmission upon THz irradiation.

In solids with impurity states or in narrow-gap insu-

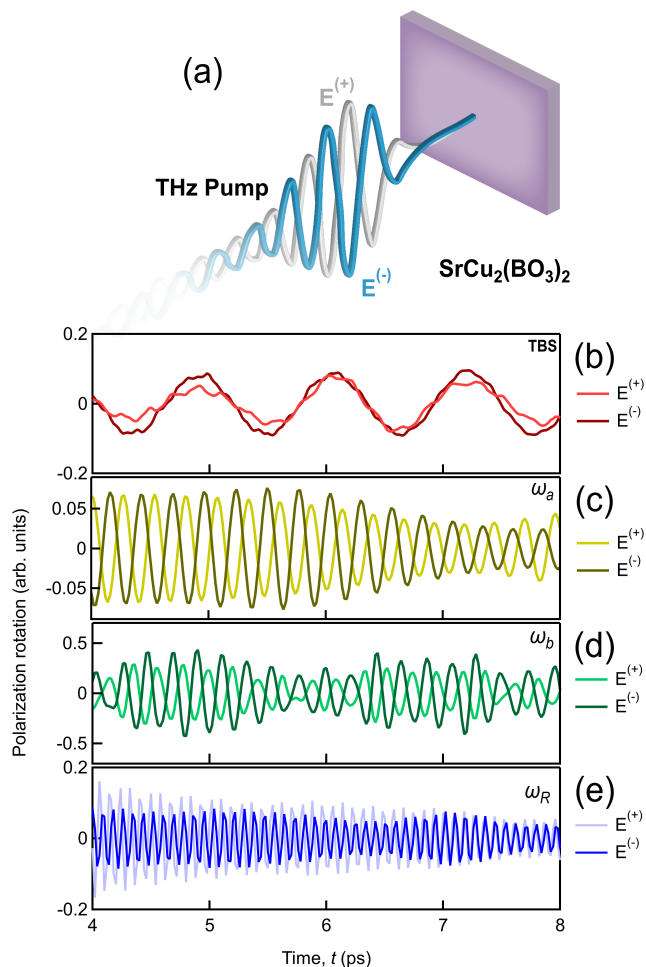


FIG. 10. **Pump polarity inversion.** (a) Representation of two THz pump pulses with inverted electric-field polarities, $E^{(+)}$ and $E^{(-)}$. (b-e) Comparison of the dynamics of the magnetic and lattice modes for these two pump polarities.

lating systems, an intense THz pulse can generate carriers through impact ionization or tunneling processes [57, 69], whose dynamics are confined to the duration of the THz pump pulse (i.e. a few picoseconds). Carrier excitation can generate vibrational or spin modes through a displacive process if the excitation dynamics are shorter than half an oscillation period of the mode [53, 54]. However, the measured $\Delta T/T$ is not compatible with this scenario: no free carriers are excited and therefore it is self-evident that displacive excitations play no role in the phenomenon we have observed. Taken together with the evidence presented in Sec. III, this result further reinforces the magnetophononic mechanism.

The $\Delta T/T$ dynamics shown in Fig. 11 can be fitted by a single exponential with a time constant of $\tau = 8.3$ ps (solid blue line), and thus can be ascribed to a slight increase in temperature arising from the relaxation of lattice phonons. One may estimate the maximum increase in temperature due to THz irradiation as being less than 1 K, based on the low-temperature specific heat

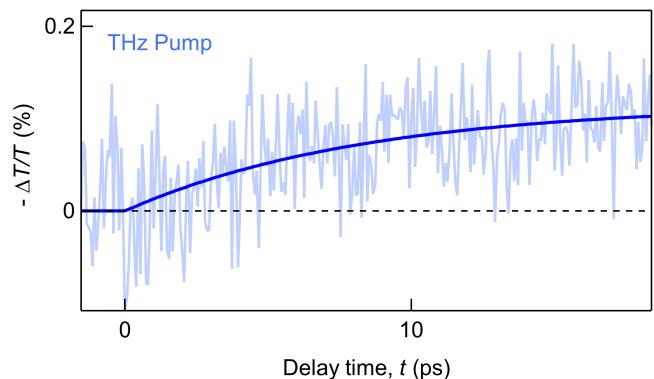


FIG. 11. **Transmission modulation.** NIR modulation of the THz transmission measured in $\text{SrCu}_2(\text{BO}_3)_2$ under the same experimental conditions as the NIR polarization rotation shown in Fig. 1(c). The blue solid line is a fit to the functional form $1 - e^{-t/\tau}$ with $\tau = 8.3$ ps.

of 5 J/mol/K [70]. The decrease of the NIR transmission with increasing temperature is consistent with the fact that the steady-state NIR transmission decreases by approximately 50% upon heating from 4 K to 300 K.

Appendix G: Phonon modulation of magnetic interactions

We have performed a hierarchy of DFT calculations in order to obtain quantitative estimates of the effects of the driven IR phonons on the magnetic system in $\text{SrCu}_2(\text{BO}_3)_2$.

1. DFT calculations at equilibrium

First we used Quantum Espresso [61] to compute the total lattice and magnetic energies of $\text{SrCu}_2(\text{BO}_3)_2$ at equilibrium. For these calculations we worked in the structural unit cell of the system, which is tetragonal and contains 44 atoms (of which 8 are Cu atoms) in two ‘‘Shastry-Sutherland’’ layers. The electron-ion interactions were modelled using pseudopotentials from the curated SSSP library [71, 72]. The plane-wave cut-off was set at 750 eV (6000 eV for the charge density) and for sampling of the Brillouin zone we used a $6 \times 6 \times 6$ k -point grid. Structural relaxation was continued until each component of the force acting at every atom was less than 0.0025 eV/Å and the pressure (defined as $\frac{1}{3} \text{Tr}[\langle \hat{\sigma} \rangle]$, with $\langle \hat{\sigma} \rangle$ being the stress tensor) was below 0.5 kbar. These parameters ensure errors smaller than 1 meV/atom within the total energy and, more importantly, smaller than 1 K on the magnetic interactions (which depend only on total-energy differences, and thus converge faster and better than do the total values). By comparing the energies of different spin configurations computed with the

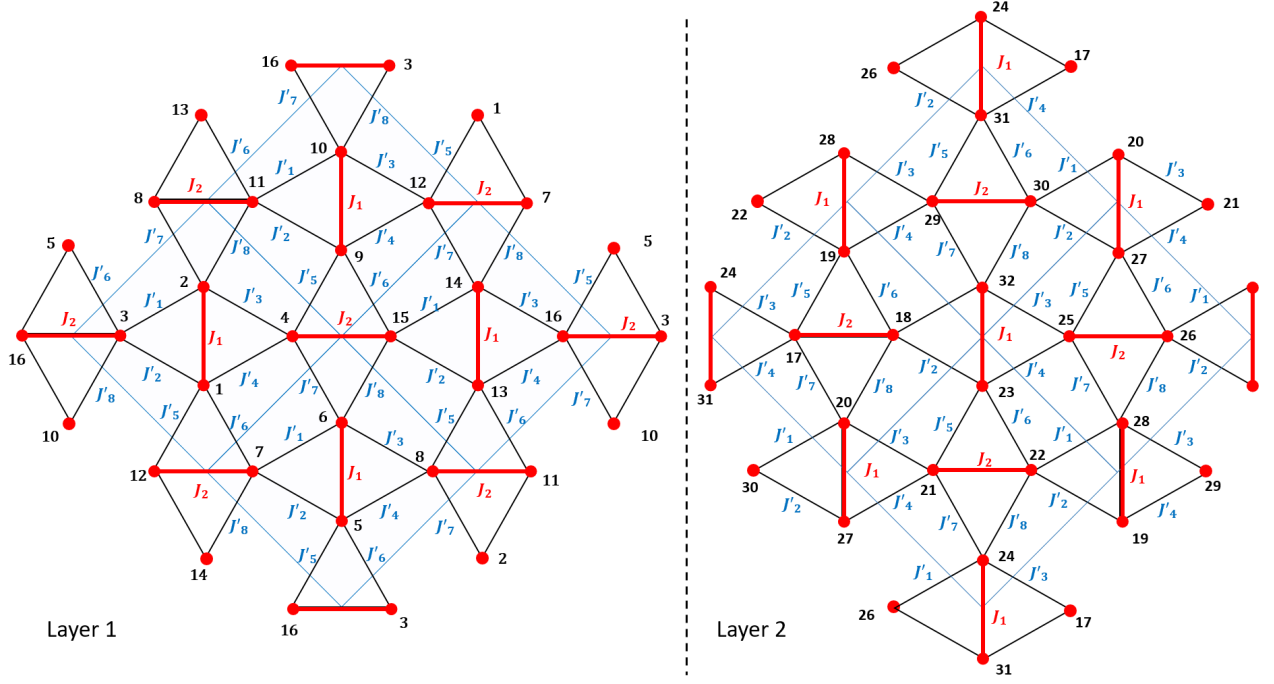


FIG. 12. **Frozen-phonon density-functional theory.** Symmetry-related magnetic interaction parameters in the spin network obtained for an arbitrary “frozen” configuration of the phonons in $\text{SrCu}_2(\text{BO}_3)_2$. Red dots represent the $S = 1/2$ spins at the Cu^{2+} sites in $\text{SrCu}_2(\text{BO}_3)_2$. For every normal mode of the lattice, the system has two different values of the intradimer interaction, J_1 and J_2 (red lines), and eight different interdimer interaction terms, J'_1, J'_2, \dots, J'_8 (black). Shown are the 2×2 supercells in each of the two layers of the structural unit cell (a total of 32 magnetic sites) required to obtain enough independent spin configurations to determine all 11 unknown parameters.

same relaxed structure, we fixed the value of the effective Hubbard term to $U = 11.4$ eV by reproducing the interaction parameters $J = 84.0$ K and $J' = 49.7$ K [63]. The lattice parameters we obtain for this value of U , the $T = 0$ DFT + U structure, agree with the measured low-temperature structure of $\text{SrCu}_2(\text{BO}_3)_2$ [73] to within 1% for the a and b axes and 3% for the c axis. The Born effective charges, Z_{eff}^i , used in Sec. III to estimate the maximum displacements, δ_m , were computed for the system in the AFM configuration using the PHONON module of Quantum Espresso and the PBE functional [62].

2. DFT calculations for frozen phonons

In order to extend our DFT calculations to include the nonequilibrium atomic configurations in the presence of lattice excitations, we first made a phonon symmetry analysis of the different interatomic paths. From this we deduced that the most general magnetic state in the presence of a phonon distortion q_t is characterized by ten different interaction parameters in the unit cell, two values of $J(q_t)$ and eight of $J'(q_t)$, as shown in Fig. 12.

To compute this number of unknown parameters, it is necessary to work on a $2 \times 2 \times 1$ supercell, meaning to use four of the basic magnetic unit cells of $\text{SrCu}_2(\text{BO}_3)_2$. In these supercell calculations we reduced the k -point grid to $2 \times 2 \times 3$, and verified that this sampling density provided essentially equivalent results.

We performed total-energy calculations for the lattice structures obtained by systematic displacement of all atoms according to the normal coordinates of the strongest two phonon modes measured in experiment [Fig. 7(a)], q_a at $\omega_a = 3.80$ THz and q_b at $\omega_b = 4.60$ THz. While it is possible to include many more of the phonons observed in App. B, here we have focused rather on optimizing our treatment of the time and frequency domains. For each distorted structure, we computed the electronic ground state as a function of the displacement amplitudes of the two phonons and for 11 different configurations of up- ($S_z = 1/2$) and down-oriented spins ($S_z = -1/2$), from which we obtained 11 linearly independent equations in order to determine all the interaction parameters in the system. This process is represented in Table I for one set of 11 spin configurations in Layer 1 of Fig. 12 and the corresponding equations are

TABLE I. Eleven independent spin configurations used for one determination of the magnetic interaction parameters. Columns from 1 to 16 are the magnetic sites shown in Layer 1 of Fig. 12. 1 denotes an up-spin ($S_z = 1/2$) and -1 a down-spin ($S_z = -1/2$).

Config. #	Magnetic site															
	1	2	3	4	5	6	7	8	9	10	11	12	13	14	15	16
1	-1	-1	1	1	-1	-1	1	1	1	1	-1	-1	1	1	-1	-1
2	-1	1	-1	-1	1	1	-1	-1	-1	-1	1	1	-1	-1	1	1
3	1	1	-1	-1	1	1	-1	-1	1	-1	1	1	-1	-1	1	1
4	-1	1	-1	-1	1	-1	-1	1	1	-1	-1	1	-1	1	1	1
5	-1	-1	1	1	-1	-1	1	1	-1	-1	1	1	-1	-1	1	1
6	-1	-1	-1	1	-1	-1	1	1	-1	-1	1	1	-1	-1	1	1
7	-1	-1	1	1	-1	-1	1	1	-1	-1	1	1	-1	1	1	1
8	-1	-1	1	1	-1	-1	1	1	-1	-1	1	1	-1	-1	1	-1
9	-1	-1	1	1	-1	-1	1	1	-1	1	-1	-1	1	-1	-1	1
10	-1	-1	1	1	-1	-1	1	1	-1	1	1	-1	1	-1	-1	-1
11	-1	-1	1	1	-1	-1	1	1	1	-1	1	-1	-1	1	-1	-1

$$\begin{aligned}
E(1) &= E_0 + 4J_1 + 4J_2 - 6J'_1 - 2J'_2 - 6J'_3 - 6J'_4 - 6J'_5 - 6J'_6 - 6J'_7 - 2J'_8, \\
E(2) &= E_0 + 4J_1 + 4J_2 - 2J'_1 - 6J'_2 - 6J'_3 - 6J'_4 - 6J'_5 - 6J'_6 - 2J'_7 - 6J'_8, \\
E(3) &= E_0 + 6J_1 + 6J_2 - 4J'_1 - 6J'_2 - 6J'_3 - 8J'_4 - 8J'_5 - 6J'_6 - 6J'_7 - 4J'_8, \\
E(4) &= E_0 + 2J_1 + 2J_2 - 4J'_1 - 6J'_2 - 2J'_3 - 4J'_4 - 4J'_5 - 2J'_6 - 6J'_7 - 4J'_8, \\
E(5) &= E_0 + 4J_1 + 4J_2 - 6J'_1 - 6J'_2 - 6J'_3 - 2J'_4 - 6J'_5 - 2J'_6 - 6J'_7 - 6J'_8, \\
E(6) &= E_0 + 4J_1 + 4J_2 - 6J'_1 - 6J'_2 - 2J'_3 - 6J'_4 - 2J'_5 - 6J'_6 - 6J'_7 - 6J'_8, \\
E(7) &= E_0 + 6J_1 + 6J_2 - 8J'_1 - 6J'_2 - 6J'_3 - 4J'_4 - 4J'_5 - 6J'_6 - 6J'_7 - 8J'_8, \\
E(8) &= E_0 - 2J_1 - 2J_2 - 6J'_2 - 6J'_3 - 6J'_6 - 6J'_7, \\
E(9) &= E_0 - 2J'_1 - 6J'_2 - 6J'_3 + 2J'_4 - 2J'_5 - 6J'_6 - 2J'_7 - 2J'_8, \\
E(10) &= E_0 - 2J'_1 - 2J'_2 - 6J'_3 - 2J'_4 + 2J'_5 - 6J'_6 - 6J'_7 - 2J'_8, \\
E(11) &= E_0 - 2J_1 - 2J_2 + 2J'_1 - 4J'_2 - 4J'_3 - 2J'_4 - 2J'_5 - 4J'_6 - 4J'_7 - 2J'_8.
\end{aligned} \tag{G1}$$

The extraction of the magnetic interaction parameters is by its nature a statistical exercise, because different spin configurations lead to different local spin densities in the DFT wave function, which cause subtle differences in the results for the effective J and J' parameters. We benchmark the accuracy of our statistics by testing the magnetic interactions at equilibrium (i.e. q_a and $q_b = 0$) with 100 different spin configurations and performing a least-squares regression analysis. As we show in Table II, our results are fully consistent with the equilibrium J and J' values. The resulting statistical error on J' is 0.4 K. E_0 in Eqs. (G1) is a large constant that captures all of the nonmagnetic contributions to the calculation and cancels from the equations determining the magnetic interaction parameters.

3. DFT calculations with driven phonons

To model our experiment, in Figs. 13(a-b) we show the vectors, meaning the ensembles of atomic displacements, of the two primary IR-active phonons excited by the THz pump ($\omega_a = 3.80$ and $\omega_b = 4.60$ THz).

We performed DFT calculations of the magnetic interactions in the presence of phonon oscillations for each phonon separately, as shown in Figs. 13(c-h), and with both phonons superposed, as we show in the time series illustrated in Fig. 5(d). Considering first the individual phonons, we observe that the intradimer interactions, $J_1(q_{a,b})$ and $J_2(q_{a,b})$, have a largely quadratic dependence on $q_{a,b}$ for both phonons [Figs. 13(c-d)], suggesting that out-of-plane O atomic motions cause the predominant effects on these parameters. By contrast, most of the interdimer interactions, $J'_i(q_{a,b})$, show strong linear as well as quadratic contributions [Figs. 13(e-f)] that depend both on the interaction pathway in question and on the combination of in- and out-of-plane atomic motions. It is clear that all four difference parameters, $\Delta J'_{12}(q_{a,b})$, $\Delta J'_{34}(q_{a,b})$, $\Delta J'_{56}(q_{a,b})$, and $\Delta J'_{78}(q_{a,b})$, have strong linear contributions [Figs. 13(g-h)] that allow an efficient driving of two-triplon creation processes by the IR-active phonon oscillations (Sec. IV).

For the purposes of creating nonlinear magnetophononic phenomena in $\text{SrCu}_2(\text{BO}_3)_2$, the strongest modulation of the $\Delta J'_{i,i+1}(q_{a,b})$ interactions is produced by the 4.60 THz phonon [Fig. 13(b)]. This is due largely

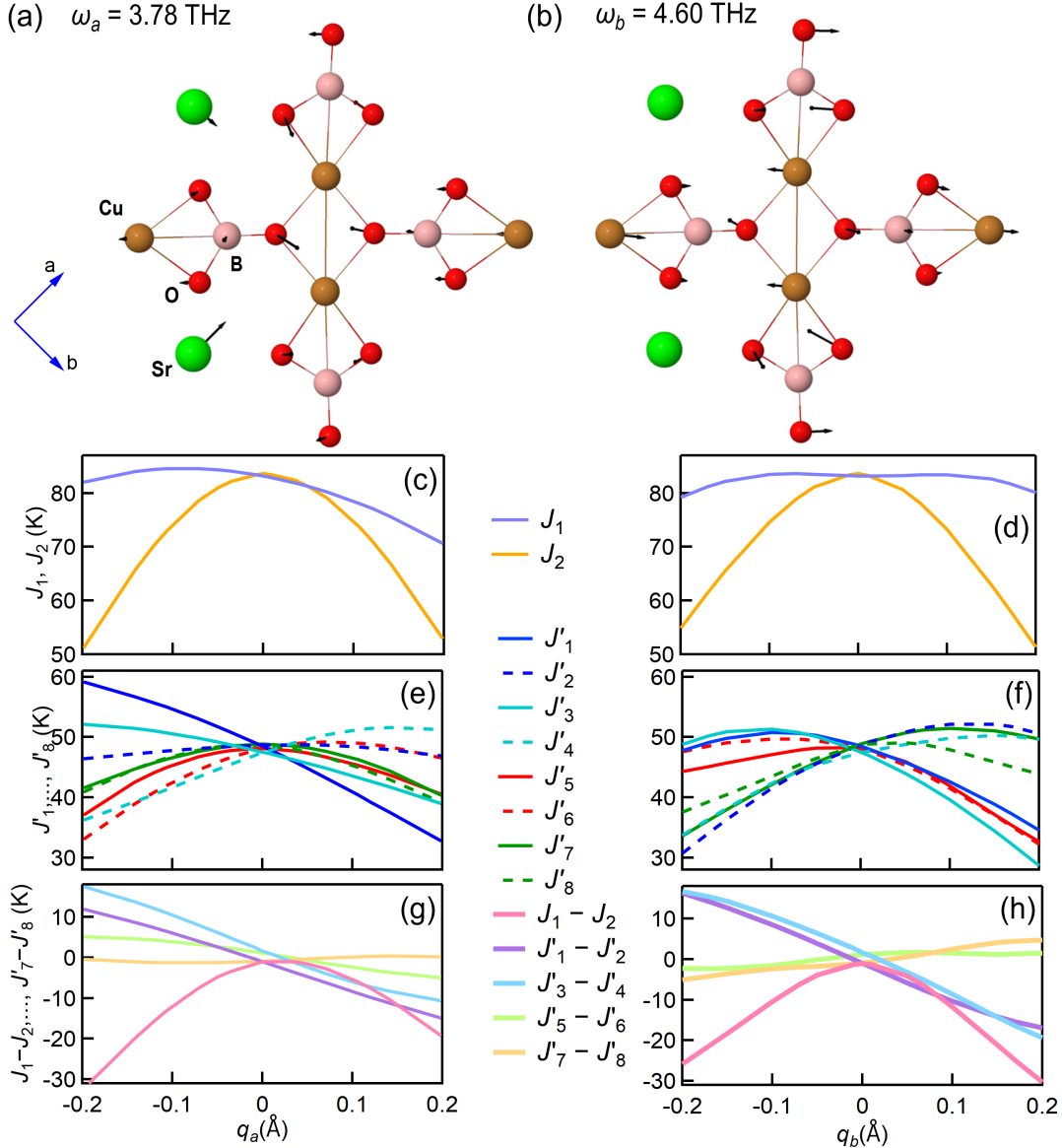


FIG. 13. **Phonon displacement vectors and calculated magnetic interaction parameters in $\text{SrCu}_2(\text{BO}_3)_2$.** (a) Atomic motions in the normal mode (q_a) of the lattice at $\omega_a = 3.80$ THz. (b) As in panel (a) for q_b at $\omega_b = 4.60$ THz. We comment that these phonon modes are not symmetric between the a' and b' axes [Fig. 1(a)], but that their doublet counterparts within each E -symmetric manifold restore this symmetry. (c-d) Intradimer interactions, J_1 and J_2 , shown as functions of the phonon displacement amplitudes. (e-f) Interdimer interactions, J'_1, \dots, J'_8 . (g-h) Differences, $\Delta J'_{12}, \Delta J'_{34}, \Delta J'_{56}$, and $\Delta J'_{78}$, between pairs of interdimer interaction parameters. The parameters shown in panels (c-f) were obtained using 11 spin configurations and, after verification of their systematic evolution, were centered on the results of Table II.

to the fact that its maximum THz-induced phonon displacement, $\delta_b = 0.17$ \AA (Sec. III), is significantly greater than that of the other phonons (at 3.80 THz we estimated the displacement $\delta_a = 0.04$ \AA). These maximum displacements are included in the calculations shown in Fig. 5, where we have computed the phonon-induced modulation of the magnetic interaction parameters as a time series based on the pulse durations of our experiment. For this calculation, we computed 285 points covering 10

ps with a time resolution of 0.035 ps, which accessed both the high- and low-frequency regimes to a sufficient degree that we obtained well-resolved results for all features, in particular the TBS peak.

Finally, we comment that an average over all our computed values of J and J' indicates that the averaged coupling ratio, $\bar{\alpha}(q_{a,b}) = \bar{J}'/\bar{J}$, increases as a function of $q_{a,b}$ for both phonon modes. This leads to the results shown in Fig. 5(g) and to the possibility of driving the static

TABLE II. Magnetic interaction parameters of $\text{SrCu}_2(\text{BO}_3)_2$ calculated using the frozen-phonon protocol with all phonon displacements set to zero.

Interaction	J_1 (K)	J_2 (K)	J'_1 (K)	J'_2 (K)	J'_3 (K)	J'_4 (K)	J'_5 (K)	J'_6 (K)	J'_7 (K)	J'_8 (K)
Strength	83.2	83.6	48.5	48.7	47.5	47.4	48.1	48.1	48.9	48.7

QPT of the spin system into the plaquette phase by using the ultrafast driving of IR phonons to increase the time-averaged coupling ratio.